Improving efficacy of therapeutics by enhancing delivery using chemical engineering

by

Hok Hei Tam

B.S. Mathematics
B.S. Chemical Engineering
Ohio State University, 2012

SUBMITTED TO THE DEPARTMENT OF CHEMICAL ENGINEERING IN PARTIAL FULFILLMENT OF THE REQUIREMENTS FOR THE DEGREE OF

DOCTOR OF PHILOSOPHY IN CHEMICAL ENGINEERING
AT THE
MASSACHUSETTS INSTITUTE OF TECHNOLOGY
FEBRUARY 2018

Signature of Author: Signature redacted
Department of Chemical Engineering
November 13, 2017

Certified by: Signature redacted
Daniel G. Anderson
Professor of Chemical Engineering
Thesis Supervisor

Accepted by: Signature redacted
Patrick S. Doyle
Robert T. Haslam Professor of Chemical Engineering
Chairman, Committee for Graduate Students

Improving efficacy of therapeutics by enhancing delivery using chemical engineering

by

Hok Hei Tam

Submitted to the Department of Chemical Engineering on Nov 13th, 2017, in Partial Fulfillment of the Requirements for the Degree of Doctor of Philosophy in Chemical Engineering.

Abstract

In the past decades, many new and interesting modalities for therapeutics have been discovered, including nucleic acid therapeutics such as siRNA and mRNA. However, one of the limiting challenges in developing these technologies into medicines is delivering the therapeutics to the correct location in the body or in the cell. Furthermore, many older modalities for therapeutics, such as vaccines and chemotherapeutics, could become more efficacious with optimization of delivery. By using chemical engineering principles, we can develop better delivery methods, materials, and formulations to improve the treatment of a wide range of diseases. In this thesis, I report on applications to vaccines and cancer.

Vaccines are currently the vanguard of public health efforts; unfortunately, a wide range of diseases have no effective vaccine. This includes devastating diseases such as HIV, malaria, and others. One area of vaccination that few people have considered optimizing is the kinetics by which the vaccine is delivered. We found that using an exponential increasing dosing profile, we could produce over 7 times more antibodies compared to the current prime-boost profile using the same amount and type of vaccine. The antibodies generated were also of higher affinity. By improving antibody affinity and titer, this work may make existing vaccines for diseases such as HIV sufficiently efficacious to use in humans.

Cancer is one of the leading causes of death in both developed and developing countries, and is extremely difficult to cure due to its high variability. Furthermore, current cancer therapeutics cause severe toxicity. By delivering more of the cancer therapeutics to the tumor, we can reduce the side effects. Some tumors, because of their location, are even harder to access: brain tumors, such as glioblastoma, are protected from most drugs by the blood-brain barrier or blood-brain-tumor barrier. Circumventing these challenges allow us to develop safer and more efficacious therapies. We found that conjugates of siRNA with chlorotoxin could knock down levels of a housekeeping gene *in vitro* and *in vivo* in a mouse brain tumor model. Furthermore, we developed prostate-cancer targeting ligands that demonstrate *in vitro* efficacy and tested them *in vivo*.

Thesis Supervisor: Daniel G. Anderson
Title: Associate Professor of Chemical Engineering

Acknowledgements

Completing this Ph.D. would not have been possible without the guidance and support of many people, both in the lab and outside. It would take many pages to acknowledge all the people who have in some way helped me in this endeavor. This is only a partial list of people who deserve acknowledgement in this thesis.

To begin with, I'd like to thank Dan for taking the risk of accepting a graduate student who hadn't touched a pipette into an experimental lab. You have been a great source of advice and direction, and working in your lab has been a great experience. I'd also like to thank Bob and Angela for taking the time out of their busy schedules to serve on my committee, as well as be a sounding board for all the questions I had about grad school, life, and what to do next. Your advice and guidance were critical to getting me where I am today.

I started in the Anderson lab having no wet lab experience outside of high school chemistry. The postdocs and other graduate students in lab were the ones who taught me everything I know about experimental biology, from how to hold a pipette to how to hold a mouse. In particular, I'd like to thank Vera Ruda, Roman Bogorad, and Jeisa Pelet, among others for guiding me during the early days of my PhD. Thank you for your patience; I could not have done this without you. The best part of lab was the people, and I'd like to thank all the people I've worked with in the Langer and Anderson labs who have made it such a great experience throughout these five years: Vera Ruda, Roman Bogorad, Hao Yin, Jeisa Pelet, Omar Khan, Josh Doloff, Arturo Vegas, Omid Veiseh, Kevin Kauffman, Jimmy Kaczmarek, Owen Fenton, Asha Patel, Kun Xue, Kaitlyn Sadtler, Derfogail Delcassian, Matt Webber, Danya Lavin, Rose Kanasty, Abel Cortinas, Lisa Volpatti, Amanda Facklam, Luke Rhym, Karsten Olejnik, Elena Smekalova, Yulia Rybakova, Natasha Nukolova, Mikhail Nesterchuk, Anna Fefilova, Piotr Kowalski, Faryal Mir, Mike Chen, Jung Yang, and others. I also worked with a wide range of people outside the lab, and I'd also like to thank them for their support and advice. These include Darrell Irvine, Herman Eisen, Arup Chakraborty, Maria Foley, Mariane Melo, Victor Koteliansky, Alex Majouga, and Timofei Zatsepin. During my PhD, I also had the opportunity to work with undergraduate and high school researchers in lab. I'd like to thank Gordon Goodwin, Siddarth Guha, and Milica Markovic in particular. It was a pleasure working with you and I'm sure you will all do great things in life.

Last but definitely not least, I'd like to thank my family for their support. Brooke, thank you for leaving your great job at Ford, marrying me, and doing a PhD at MIT. I am grateful for all the love and support you've given me these past five years. I'd also like to thank my parents Mo Yee and Kwok Kwan and my brother Tze Hei for supporting me all these years and encouraging me to do this. This would not have been possible without you.

Table of Contents

List of Figures

List of Tables

Abbreviations

Ab – Antibody
ACTB – Beta Actin
ANOVA – Analysis of Variance
ATCC – American Type Culture Collection
BNAb – Broadly neutralizing antibody
BSA – Bovine serum albumin
CAR – Chimeric Antigen Receptor
CD – Cluster of Differentiation
CHO – Chinese hamster ovary
CTX – chlorotoxin
Cy5.5 – Cyanine 5.5
CYCLOPS - Copy number alterations yielding cancer liabilities owing to partial loss
DMSO – Dimethylsulfoxide
DNA – Deoxyribonucleic acid
Dox – Doxorubicin
ELISA – Enzyme-linked immunoassay
Exp-dec – exponentially decreasing
Exp-inc – exponentially increasing
FDA – Food and Drug Administration
FDC – Follicular dendritic cell
FITC – Fluorescein isothiocyanate
GalNAc – Galactose-N-acetaldehyde
GC – germinal center
GFP – Green fluorescent protein
gp – glycoprotein
HEK – Human embryonic kidney
HIV – Human immunodeficiency virus
HRP – Horseradish peroxidase
IC – immune complex
Ig – Immunoglobulin
KD – Knockdown
LN – lymph node
Luc – Luciferase
MALDI-TOF – Matrix-assisted Laser Desorption/Ionization-Time of Flight
MED – Minimum effective dose
MHC – Major histocompatibility class
MMP – Matrix metallopeptidase
MPLA – Monophosphoryl lipid A
MRI – Magnetic Resonance Imaging
mRNA – messenger RNA
MS – Mass Spectrometry
MTD – Maximum tolerable dose
NS – Not significant
PBS – Phosphate-buffered saline

PD – Pharmacodynamics
PE – Phycoerythin
PEG – polyethylene glycol
PEI – Polyethylimine
PK – Pharmacokinetics
PNA – Peanut agglutinin
PSMA – Prostate specific membrane antigen
RNA – Ribonucleic acid
RP-HPLC – Reverse phase High Performance Liquid Chromatography
SHM – somatic hypermutation
si/siRNA – small interfering RNA
Tfh – T-follicular helper cell
TMB - 3,3',5,5'-Tetramethylbenzidine

Chapter 1: Introduction

Overview

The central dogma of biology is as follows: DNA is transcribed into RNA, which is translated into protein, which has a wide range of activities. From ancient times until now, people have focused on interfering somewhere along this path (knowingly or unknowingly) to treat disease and improve health (1). This process began with plants that contained beneficial small molecules, and has now advanced to small molecule inhibitors of specific proteins, nucleic acid therapies that can modulate a wide variety of genes, protein therapies that interact and signal with other proteins, and even cell-based therapies that can replicate and make decisions (2–5). However, despite our advances in creating new and ever more potent therapeutic modalities, a basic challenge remains that we have yet to be able to overcome: the challenge of directing the therapeutic to the right location in the body or even in the cell (6). This is what the field of drug delivery has set out to do, and the challenges are manifold.

Most small molecule drugs permeate the entire body, and if the drug acts outside of the targeted location, there could be toxicities or other side effects (6). As an example, chemotherapeutics are drugs that target physiological processes that affect rapidly-dividing cells the most (7). This indeed causes irreparable damage to cancer cells; however, it also wipes out certain immune cell populations, such as neutrophils, leading to deadly infections (8). It also affects hair stem cells, leading to the telltale balding of chemotherapy patients (8). The ability to direct chemotherapeutics only to cancer cells would revolutionize cancer treatment—higher doses would lead to more complete eradication of the tumors without causing toxic side effects.

Instead of causing toxic effects, some drugs lose their efficacy when they are not in the correct location. Nucleic acid drugs include small interfering RNAs that can knock down any gene, mRNAs that can upregulate any protein, and DNA gene therapies that can insert new genes or fix current ones (3). However, if these therapeutics do not reach the cytoplasm (RNA) or nucleus (DNA) of sufficient numbers of diseased cells, they will not have any effect (9). There are many barriers in the way of these therapeutics: first, the nucleic acid, typically injected intravenously, needs to survive the bloodstream and avoid endonucleases that seek to protect your body from viruses. Secondly, the molecule must leave the bloodstream at the correct site to enter the tissue of interest. Thirdly, the molecule must somehow identify the correct cell type. Lastly, the molecule must cross one or more lipid membranes in order to get inside the cell or nucleus (9). This is especially difficult for nucleic acid molecules as they are heavily negatively charged, which renders them unable to cross lipid membranes. Because of these challenges, very few of these therapeutics have reached clinical stage and none of these types of therapies have yet been approved by the FDA (10).

Besides simple molecular therapies, these ideas can also be used to improve more complex therapeutic interventions, such as cell therapies and vaccinations. In the case of vaccinations, understanding where, when, and how the antigen is passed around in the system allows one to develop better ways to induce antibodies as well as cytotoxic T-cell responses against infectious diseases and cancer(11, 12). Longer or controllable dosage forms of drugs lead to better patient experiences and can increase efficacy and safety. Furthermore, cell therapies need to be directed to the correct location in order to have maximal effect and minimal off-target effects. As an example, chimeric antigen receptor

T (CAR-T) cells are effective and have been approved for certain lymphomas, but have been associated with a wide range of off-target toxicities that can even lead to death (13, 14).

In summary, delivering therapeutics to the correct location at the right time is a great challenge for many therapeutics, ranging from simple small molecules to more complex proteins and even cell-based therapies. Successfully doing so would allow many novel therapeutics to reach their full potential. In this Introduction, I will review fundamental principles of drug delivery, highlight examples of current methods of drug delivery, and examine new ways to deliver certain types of compounds.

Principles of Drug Delivery

Drug delivery is the field of getting therapeutics to where they are needed in the body. We can consider this through the dimensions of space and time. Spatially, we are concerned with where the therapeutic reaches in the body. This could include delivery to certain tissues, organs, or even within certain cells. Temporally, we are interested in how concentrations build and decrease in certain parts of the body, and how we can optimize these profiles. Many of these ideas have been derived from pharmacology.

Pharmacokinetics (PK) is the study of how drugs move within the body, and pharmacodynamics (PD) is the study of how drugs are transformed and act within different places (15). By studying ways of modifying PK/PD properties of drugs, we can change where they go. These types of studies are typically done by analyzing distribution within animals *in vivo* using drug labeled with radioactive elements, fluorescent molecules, or antibody tags (16). Other measures of interest include the kinetics of the drug in key compartments of the body, such as the bloodstream.

The goal of modifying delivery and changing PK/PD is to improve the therapeutic window. This is the range of doses between the minimum effective dose (MED) of the drug and the maximal tolerable dose (MTD) of the drug. There are two ways of doing so: decreasing the efficacious dose, or increasing the MTD. Using cancer as an example, if we double the amount of the drug that reaches the tumor, we can halve the efficacious dose, which greatly improves the therapeutic window (17). Likewise, having more of a drug circulating in an encapsulated form could reduce kidney toxicity without changing the effective dose (18).

Strategies for Spatial control of therapeutics

Broadly speaking, there are two routes one could use for delivering therapeutics: firstly, we can release a compound locally, in order to have maximum concentration at some area of the body. Secondly, we could consider introducing a compound in some other part of the body. This could be done orally, in the bloodstream, or into some other compartment: muscle, under the skin, the peritoneum, or even spinal cord. Each of these methods have tradeoffs between invasiveness and ability to get drug into the desired location(19, 20). Furthermore, each has different kinetics in terms of how long and when therapeutics are delivered.

Oral delivery has traditionally been fairly popular, due to its ease of administration. However, compounds undergo metabolism in the microbiome and the liver, and thus may change (21). Furthermore, bloodstream availability is often poor, especially for larger molecules (22). Direct injection into the bloodstream has immediate bloodstream bioavailability, but also increases biodistribution to organs such as liver, kidney, and spleen, which may experience toxicity (23).

Many methods have been invented to deliver therapeutics to the correct location or modify its biodistribution. This has been useful in a wide variety of applications, ranging from cancer to wound healing(7, 24). In this section, I review some of the more common systems that have been tried in the past. These include encapsulation inside or conjugation onto nanoparticles, chemical modification/conjugation of ligands, and a variety of methods for local delivery.

Nanoparticle carriers

A wide variety of therapeutics can be encapsulated into or onto nanoparticles. These include small molecules, nucleic acids, and proteins (25–27). Nanoparticles are able to change the size, shape, and chemical interactions of the therapeutic relative to its environment, thus enabling delivery to different or more selective locales than the drug alone (28, 29). In some cases, nanoparticles can also protect the drug from degradation (9). Thus, encapsulation in nanoparticles has been adopted as one of the primary methods for modulating the biodistribution of a wide variety of therapeutics.

Nanoparticles come in a wide variety of shapes and sizes, and can be made from many different types of materials. Some of the more common nanoparticles are gold nanoparticles, magnetic nanoparticles, quantum dots, polymer nanoparticles, and liposomes. Gold nanoparticles come in a wide range of shapes, including spheres, rods, shells, and cages (30). Because of its inert nature, gold nanoparticles are well tolerated and non-toxic(31). They can be manufactured using a one-pot method and react with sulfur moieties, which allows for a wide range of bioconjugation strategies (31). They can be functionalized with a wide range of molecules, including antibiotics, cancer drugs, and larger molecules such as nucleic acids and antibodies (30, 31). Besides therapeutic

moieties, they can be coated with targeting molecules to further direct them to certain locations in the body (30, 32). Furthermore, in the context of cancer, they can be irradiated with radio- or microwaves to generate heat, which can be used to locally ablate cancer (32). These systems are already in clinical trials (32).

Magnetic nanoparticles are typically made from superparamagnetic iron oxide nanocrystals (33). They maintain magnetic properties, and thus can be guided with magnets or used as contrast agents for MRIs (34). Magnetic nanoparticles can be synthesized with a wide range of methods, including mechanical attrition and chemical synthesis (35). After synthesis, in order to protect the particles and provide reactive handles for bioconjugation, magnetic nanoparticles are typically coated with polymers or lipids. Typical coatings include PEG, chitosan, dextran, PEI, and phospholipids (for formulation into liposomes and micelles) (35). Drug and targeting moieties can then be added to the coatings to create a therapeutic or diagnostic agent (33, 35). A wide range of therapeutic modalities primarily for use in cancer treatment have been attached to magnetic nanoparticles, including small molecules, proteins, and nucleic acid drugs (34). For applications close to the surface, magnetic field gradients can be used to guide the nanoparticles towards a target (34). As contrast agents, magnetic nanoparticles have been used to illuminate tumors with MRI due to its effect on local proton relaxation (34). They can be targeted using the enhanced permeation and retention effect, where tumors exhibit leaky vasculature and accumulate nanoparticles, and also through the direct conjugation of active targeting moieties, such as antibodies and other proteins (34).

Polymer nanoparticles have also been used for drug delivery. They can be made from a wide range of polymers, ranging from non-biodegradable polymers such as

polymethylmethacrylate and polystyrene, to biodegradable polymers including polylactic acid and chitosan (25, 36). Because of the wide range of polymers used and their differing biological activities, toxicity can be a problem for certain types of polymeric nanoparticles, especially those constructed out of non-biodegradable materials (36). Polymeric nanoparticles can be made into a wide range of shapes and sizes, including spherical particles, thin rods, polymer brushes, and micelles (36). Their versatility allows for encapsulation or conjugation of a wide range of therapeutic entities, including small molecules, proteins, and nucleic acids (36). For nucleic acid delivery in particular, cationic polymers enable the negatively-charged nucleic acids to form stable complexes. These complexes protect the nucleic acids and also enhance transfection efficacy. In order to change the pharmacokinetics of the polymers, the nanoparticle size and surface chemistry/charge can be modified. Size plays a major role in nanoparticle clearance: nanoparticles less than 10 nm can be filtered out by the kidney, and nanoparticles greater than 200 nm are typically removed by phagocytosis (36). Hence, nanoparticles of sizes between these ranges can circulate for a longer period of time and deliver therapeutics. Changing the surface chemistry by modifying the surface charge or coating with PEG varies how much the nanoparticle interacts with cells (36). Furthermore, attaching targeting moieties to the nanoparticles can also increase biodistribution to an organ of interest (37). This has been used for a wide range of cancer therapeutics and some targeted towards organs such as the brain and the liver (37).

Liposomes and lipid nanoparticles also have been successful in drug delivery. These have typically been made from natural phospholipids in order to mimic natural vesicles and reduce potential toxicity (38). Most liposomes and lipid nanoparticles are

roughly spherical, but their size can be controlled through differences in synthesis methodology. Liposomes can also be formed with many layers (38). Liposomes and lipid nanoparticles can be synthesized through emulsion, extrusion, high pressure thin film hydration, evaporation, or microfluidic devices (38). Their properties are strongly dictated by the lipid composition and any additives, including cholesterol, PEGylated lipids, and polymers (38, 39). Like polymer nanoparticles, size plays a large role in liposomal clearance, and the effective size ranges are similar to polymeric nanoparticles (38). Liposomes and lipid nanoparticles can encapsulate both hydrophobic and hydrophilic drugs, including chemotherapeutics, other small molecules, proteins, peptides, siRNAs, antisense, oligonucleotides, DNA, mRNA, and other therapeutics (38, 39). Using modified phospholipids with reactive groups, targeting ligands such as antibodies and small molecules can be incorporated on the surface to target these therapeutics to specific organs or to cancerous tissue (38, 39). Liposomal therapies for cancer and rare diseases are in clinical trials already and some of them are currently used in the clinic (38).

Direct conjugation

Besides formulating into nanoparticles that can deliver in a targeted fashion, therapeutics can also be attached directly to other types of molecules to improve pharmacokinetics. Some of these include attaching therapeutics to circulating proteins or PEG to improve residence time and to targeting ligands to change the biodistribution. Attaching PEGs and certain polymers to therapeutics can increase their circulation time as well as prevent immunological recognition or degradation (40). These tactics have been used to great effect on a wide range of enzyme therapies for rare disease and cancer in the clinic, as the increased circulation reduces the frequency of dosing required

to maintain the same amount of enzymatic activity (40). Furthermore, PEGylated versions of some enzymes of bacterial origin do not provoke the same immune reaction as native enzyme, allowing their usage in patients with hypersensitivity reactions to the enzyme (40). PEGylation of certain signaling molecules, such as G-CSF, IFNγ, and even insulin have been used to develop longer-acting forms that still are capable of retaining signaling capabilities (41). Besides PEGylation, small molecule drug conjugates to carrier proteins that have long circulation half-lives have also been developed. These primarily involve albumin, the most abundant protein in serum (42). Not only does conjugation of drug to albumin improve circulation time, solubility, and tolerability, albumin is preferentially taken up by tumors, inflamed areas, and the liver (42). These properties have made it a useful target moiety for therapeutics against diseases such as hepatocellular carcinoma and rheumatoid arthritis (42).

Therapeutics can also be directly conjugated to a targeting ligand to deliver to specific locations. These include proteins, antibodies, peptides, aptamers, and even small molecules. One well-known example of this type of system are antibody-drug conjugates (ADCs). These are primarily used for cancer therapy, where targeted delivery of chemotherapeutics to the tumor alone reduces side effects associated with off-target toxicity (43, 44). Typically, multiple drugs are conjugated to one antibody in order to deliver a higher level of payload (44). Some ADC systems also include cleavable linkers that release the drug in the tumor environment (43). ADCs against HER2 and CD30 have already been approved for use in the clinic (43). Besides ADCs, another area where conjugates have shown promise is in the delivery of siRNA to cells. One of the most clinically-advanced siRNA platforms involves using a small molecule ligand (GalNAc)

directly conjugated to siRNA to deliver to the liver (45). Along with stabilizing chemistries that make it highly efficacious while retaining a low amount of toxicity, this type of platform is already in later-stage clinical trials (45). Besides GalNAc, other targeting ligands have also been attempted for use with similar siRNA systems, including a wide range of integrin ligands for tumors, CpG ligands for immune cells, and aptamers for prostate cancer (46).

Receptor targeted systems have also been found useful for targeting the brain, which is naturally protected by the blood-brain barrier. The blood brain barrier is a system of tight junctions that prevent many types of molecules from entering the brain through the endothelium (47). However, conjugates of therapeutics to antibodies against the insulin receptor or transferrin receptor have allowed for delivery of these therapeutics into the brain parenchyma at rates competitive with small molecule drugs (48). These types of conjugates are in trials for lysosomal storage diseases, which are rare inherited disorders of lysosomal processing that lead to accumulation of waste products in the lysosome (48, 49). Enzyme replacement therapy has been successful in improving the quality of life for a wide range of patients, but the inability of these enzymes to cross the blood brain barrier prevents their use in patients with cognitive involvement (49). Besides antibodies, small molecules have also been used to deliver therapeutics to the brain: siRNA-sertraline conjugates administered intranasally have been shown to induce knockdown in the brain (50). For brain tumors, proteins such as chlorotoxin have also demonstrated efficacy in taking molecules such as chemotherapeutics and diagnostic agents across the blood brain tumor barrier (51). Fluorescently-labelled chlorotoxin is in clinical trials for glioblastoma as a surgical adjunct to help surgeons visualize the tumor margin (52).

Local delivery

Local delivery is one of the mainstays of modern drug delivery. Besides injections, there have been a wide variety of methods developed to deliver drugs locally, including microneedles, patches, and implantable devices such as pumps and polymer release systems (53). Many such systems rely on using proximal diffusion gradients to release a drug into its immediate environment in order to minimize the amount systematically in the bloodstream. These systems are already in use in the clinic, mostly for cancer therapeutics (53). An example of this is the Gliadel wafer for glioblastoma, which is situated in the tumor site after resection and releases chemotherapeutics that suppress any leftover tumors (53). This allows local concentrations of the drug to be highest at the tumor site and lower elsewhere in the body where toxicity could occur.

Strategies for temporal control of therapeutics

Another aspect of drug delivery is changing the kinetics of delivery. Traditionally, this has been done to slow down release to reduce administration frequency, but recently, other methods have been developed to modulate the profile. For orally-delivered drugs, there have been a variety of systems developed to decrease the rate of passage and prolong the release of drug. Local delivery systems have also been deployed with polymers that either degrade or swell over time, slowly releasing molecules. Recently, newer methods of controlled release have been developed that are responsive to external stimuli.

Gastrointestinal systems

Oral delivery of pharmaceuticals has been the mainstay of the pharmaceutical industry. However, in order to maintain consistent concentrations of therapeutics,

frequent dosing may be needed. In order to overcome this limitation, several types of systems have been invented to increase the transit time through the GI tract and lengthen dosing (54, 55). Some of these use mucoadhesive coatings, which are generally made from polymers that interact with intestinal mucus (54). These interactions can be through hydrogen bonds or van der Waals forces, although some may actually interact through binding with receptors as well (54). Mucoadhesive coatings significant slow transit time and allows for hours of drug release (54).

Other systems use physical properties of the stomach to keep a drug delivery device in the stomach for a prolonged period of time. These include systems that swell in acidic conditions to sizes that prevent the device from leaving the stomach (54). This allows the drug to be slowly released until the device is eroded. Floating systems have also been developed that float in the stomach and thereby avoid transport out of the stomach (55). The floatation device can be designed to have low density, but other systems have been designed to self-inflate upon hitting the acidic environment of the stomach by generating carbon dioxide gas (55). Such systems are able to stay afloat and continue to release drug on the order of days (55).

Passive local systems

Polymeric systems have been widely used to change the release profile of a wide range of therapeutics. They have been fashioned in a wide range of shapes and sizes, ranging from microparticles and gels to films and rods. Microparticle drug release systems were developed to create injectable depots for long-lasting release of drugs using polymers that slowly degrade (56). Besides the polymer, the shape and size of these materials also play a large role in how they degrade and release drug (56). These

technologies are already clinical stage, and have been used to encapsulate a wide range of drugs, ranging from luteinizing hormone releasing hormone to cancer drugs such as doxorubicin and paclitaxel (56). Although most microparticle systems are injected, some can also be formulated as inhalable systems in order to deliver drugs to the lung (57). These have been used in the clinic to treat lung cancer, lung transplant rejection, and cystic fibrosis(57). Currently, these formulations allow drugs to be released at a fairly consistent rate for months (56).

Besides microparticles, a wide range of other types of local release systems have also been developed. Many of these are implantable systems with a reservoir of drug held within. Devices such as osmotic pumps, microchannel systems, membrane-base devices, microneedles, and others have been developed that hold the drug within the system (53, 58). Such systems can be implanted or affixed to the skin in easily-accessible locations and release drugs systemically for years in certain cases (58). These systems have primarily been used for small-molecule drugs (58). Some of the ones in the clinic currently are devices that release contraceptives, other hormones, and cancer drugs (58). A wide range of devices have also been developed for ophthalmic use, primarily to release drugs for glaucoma and retinopathies (58). Drug eluting stents have also been developed that release drugs and prevent further narrowing of the blood vessel, thereby increasing the useful life of the stent (58).

Responsive systems

Most systems for sustained release function due to diffusion. However, newer methods of delivery have been developed that are capable of releasing drugs in response to certain external stimuli. Many of these responsive systems have been engineered

using chemistry that allows them to modulate release based upon presence of certain stimuli. One example of this type of system are glucose-responsive insulin delivery systems, which reduce the risk of hypoglycemia in diabetics who use insulin (59). These have typically been designed using phenylboronic acid or concanavalin A, which both bind to glucose (59). High glucose concentrations then change the conformation of a larger nanostructure and either lead to release of insulin or activation of an inactive form of insulin (59).

Electronically controlled systems have been developed that allow for release of drug upon reception of a signal (60). These microelectromechanical systems are fabricated with process similar to those used in the semiconductor industry, allowing them to be made to a very small size (60). Up to thousands of nanoliter-sized doses of drug are stabilized within individual wells in these systems, and thus can be released years after implantation upon appropriate signaling through electrical destruction of a cap material (60). Such devices are currently in clinical trials for applications including chemotherapy and osteoporosis (60).

Responsive systems have also been developed using biological circuitry to control delivery. Because cells already are capable of controlling secretion in response to stimulus, using them to manufacture or deliver drugs helps ensure that drugs are delivered to the right location at the right time. However, introducing other cells in the body can lead to immune attack and destruction, so methods are needed in order to make these systems useful (61). As an example, new biomaterials have been developed that are capable of shielding cells from the immune system (61). These materials have been used to encapsulate islet cells that naturally secrete insulin in response to glucose (61).

Similar systems have also been developed for using hepatocytes in the case of liver failure (62).

References

1. Crick F (1970) Central dogma of molecular biology. *Nature* 227(5258):561–3.
2. Hoelder S, Clarke PA, Workman P (2012) Discovery of small molecule cancer drugs: Successes, challenges and opportunities. *Mol Oncol* 6(2):155–176.
3. Opalinska JB, Gewirtz AM (2002) Nucleic-acid therapeutics: basic principles and recent applications. *Nat Rev Drug Discov* 1(7):503–514.
4. Davidson BL, McCray PB, McCray PB (2011) Current prospects for RNA interference-based therapies. *Nat Rev Genet* 12(5):329–340.
5. Trounson A, McDonald C (2015) Stem Cell Therapies in Clinical Trials: Progress and Challenges. *Cell Stem Cell* 17(1):11–22.
6. Allen TM, Cullis PR (2004) Drug Delivery Systems: Entering the Mainstream. *Science (80-)* 303(5665). Available at: http://science.sciencemag.org/content/303/5665/1818 [Accessed September 15, 2017].
7. Iwamoto T (2013) Clinical Application of Drug Delivery Systems in Cancer Chemotherapy: Review of the Efficacy and Side Effects of Approved Drugs. *Biol Pharm Bull* 36(5):715–718.
8. Selwood K Side Effects of Chemotherapy. *Cancer in Children and Young People* (John Wiley & Sons, Ltd, Chichester, UK), pp 35–71.
9. Whitehead K a, Langer R, Anderson DG (2009) Knocking down barriers: advances in siRNA delivery. *Nat Rev Drug Discov* 8(2):129–38.

10. Lorenzer C, Dirin M, Winkler A-M, Baumann V, Winkler J (2015) Going beyond the liver: Progress and challenges of targeted delivery of siRNA therapeutics. *J Control Release* 203:1–15.

11. Tam HH, et al. (2016) Sustained antigen availability during germinal center initiation enhances antibody responses to vaccination. *Proc Natl Acad Sci U S A* 113(43):E6639–E6648.

12. Johansen P, et al. (2008) Antigen kinetics determines immune reactivity. *Proc Natl Acad Sci U S A* 105(13):5189–94.

13. Li H, Zhao Y (2017) Increasing the safety and efficacy of chimeric antigen receptor T cell therapy. *Protein Cell* 8(8):573–589.

14. Kakarla S, Gottschalk S (2014) CAR T cells for solid tumors: armed and ready to go? *Cancer J* 20(2):151–5.

15. Wright DFB, Winter HR, Duffull SB (2011) Understanding the time course of pharmacological effect: a PKPD approach. *Br J Clin Pharmacol* 71(6):815–23.

16. Rockey WM, et al. (2011) Synthesis and radiolabeling of chelator–RNA aptamer bioconjugates with copper-64 for targeted molecular imaging. *Bioorg Med Chem* 19(13):4080–4090.

17. Gelmon KA, et al. (1999) Phase I study of liposomal vincristine. *J Clin Oncol* 17(2):697–705.

18. Tollemar J, Andersson S, Ringdén O, Tydén G A retrospective clinical comparison between antifungal treatment with liposomal amphotericin B (AmBisome) and conventional amphotericin B in transplant recipients. *Mycoses* 35(9–10):215–20.

19. Huang X, et al. (2013) Effect of Injection Routes on the Biodistribution, Clearance,

and Tumor Uptake of Carbon Dots. *ACS Nano* 7(7):5684–5693.

20. Boelaert JR, et al. (1989) Comparative pharmacokinetics of recombinant erythropoietin administered by the intravenous, subcutaneous, and intraperitoneal routes in continuous ambulatory peritoneal dialysis (CAPD) patients. *Perit Dial Int* 9(2):95–8.
21. Swanson HI (2015) Drug Metabolism by the Host and Gut Microbiota: A Partnership or Rivalry? *Drug Metab Dispos* 43(10):1499–504.
22. Goldberg M, Gomez-Orellana I (2003) Challenges for the oral delivery of macromolecules. *Nat Rev Drug Discov* 2(4):289–295.
23. Yang L, et al. (2017) Comparisons of the biodistribution and toxicological examinations after repeated intravenous administration of silver and gold nanoparticles in mice. *Sci Rep* 7(1):3303.
24. Boateng JS, Matthews KH, Stevens HNE, Eccleston GM (2008) Wound Healing Dressings and Drug Delivery Systems: A Review. *J Pharm Sci* 97(8):2892–2923.
25. Soppimath KS, Aminabhavi TM, Kulkarni AR, Rudzinski WE (2001) Biodegradable polymeric nanoparticles as drug delivery devices. *J Control Release* 70(1–2):1–20.
26. Whitehead KA, et al. (2014) Degradable lipid nanoparticles with predictable in vivo siRNA delivery activity. *Nat Commun* 5:4277.
27. Moon JJ, et al. (2012) Enhancing humoral responses to a malaria antigen with nanoparticle vaccines that expand Tfh cells and promote germinal center induction. *Proc Natl Acad Sci U S A* 109(4):1080–5.
28. Li S-D, Huang L (2008) Pharmacokinetics and Biodistribution of Nanoparticles. *Mol Pharm* 5(4):496–504.

29. Saraiva C, et al. (2016) Nanoparticle-mediated brain drug delivery: Overcoming blood-brain barrier to treat neurodegenerative diseases. *J Control Release* 235:34–47.

30. Vigderman L, Zubarev ER (2013) Therapeutic platforms based on gold nanoparticles and their covalent conjugates with drug molecules. *Adv Drug Deliv Rev* 65(5):663–676.

31. Ghosh P, Han G, De M, Kim CK, Rotello VM (2008) Gold nanoparticles in delivery applications. *Adv Drug Deliv Rev* 60(11):1307–1315.

32. Abadeer NS, Murphy CJ (2016) Recent Progress in Cancer Thermal Therapy Using Gold Nanoparticles. doi:10.1021/ACS.JPCC.5B11232.

33. McBain SC, Yiu HHP, Dobson J (2008) Magnetic nanoparticles for gene and drug delivery. *Int J Nanomedicine* 3(2):169–80.

34. Sun C, Lee JSH, Zhang M (2008) Magnetic nanoparticles in MR imaging and drug delivery. *Adv Drug Deliv Rev* 60(11):1252–1265.

35. Veiseh O, Gunn JW, Zhang M (2010) Design and fabrication of magnetic nanoparticles for targeted drug delivery and imaging. *Adv Drug Deliv Rev* 62(3):284–304.

36. Banik BL, Fattahi P, Brown JL (2016) Polymeric nanoparticles: the future of nanomedicine. *WIREs Nanomed Nanobiotechnol* 8:271–299.

37. Ulbrich K, et al. (2016) Targeted Drug Delivery with Polymers and Magnetic Nanoparticles: Covalent and Noncovalent Approaches, Release Control, and Clinical Studies. *Chem Rev* 116(9):5338–5431.

38. Kraft JC, Freeling JP, Wang Z, Ho RJY (2014) Emerging research and clinical

development trends of liposome and lipid nanoparticle drug delivery systems. *J Pharm Sci* 103(1):29–52.

39. Allen TM, Cullis PR (2013) Liposomal drug delivery systems: From concept to clinical applications. *Adv Drug Deliv Rev* 65(1):36–48.

40. Greenwald RB, Choe YH, McGuire J, Conover CD (2003) Effective drug delivery by PEGylated drug conjugates. *Adv Drug Deliv Rev* 55(2):217–250.

41. Pasut G, Veronese FM (2007) Polymer-drug conjugation, recent achievements and general strategies. *Prog Polym Sci* 32(8–9):933–961.

42. Kratz F (2008) Albumin as a drug carrier: Design of prodrugs, drug conjugates and nanoparticles. *J Control Release* 132(3):171–183.

43. Beck A, Goetsch L, Dumontet C, Corvaïa N (2017) Strategies and challenges for the next generation of antibody–drug conjugates. *Nat Rev Drug Discov* 16(5):315–337.

44. Alley SC, Okeley NM, Senter PD (2010) Antibody-drug conjugates: Targeted drug delivery for cancer. *Curr Opin Chem Biol* 14(4):529–537.

45. Kanasty R, Dorkin JR, Vegas A, Anderson D (2013) Delivery materials for siRNA therapeutics. *Nat Mater* 12(11):967–977.

46. Ming X, Laing B (2015) Bioconjugates for targeted delivery of therapeutic oligonucleotides. *Adv Drug Deliv Rev* 87:81–89.

47. Pardridge WM, Boado RJ, Farrell CR (1990) Brain-type glucose transporter (GLUT-1) is selectively localized to the blood-brain barrier. Studies with quantitative western blotting and in situ hybridization. *J Biol Chem* 265(29):18035–18040.

48. Pardridge WM (2012) Drug Transport across the Blood–Brain Barrier. *J Cereb*

Blood Flow Metab 32(11):1959–1972.

49. Platt FM, Lachmann RH (2009) Treating lysosomal storage disorders: Current practice and future prospects. *Biochim Biophys Acta - Mol Cell Res* 1793(4):737–745.

50. Ferrés-Coy A, et al. (2016) Therapeutic antidepressant potential of a conjugated siRNA silencing the serotonin transporter after intranasal administration. *Mol Psychiatry* 21(3):328–38.

51. Ojeda PG, Wang CK, Craik DJ (2016) Chlorotoxin: Structure, activity, and potential uses in cancer therapy. *Biopolymers* 106(1):25–36.

52. Franklin HL, Miller DM, Hedges T, Perry J, Parrish-Novak J (2016) Clinical development of BLZ-100 for real-time optical imaging of tumors during resection. eds Pogue BW, Gioux S (International Society for Optics and Photonics), p 96960V.

53. Wolinsky JB, Colson YL, Grinstaff MW (2012) Local drug delivery strategies for cancer treatment: Gels, nanoparticles, polymeric films, rods, and wafers. *J Control Release* 159(1):14–26.

54. Talukder R, Fassihi R (2004) Gastroretentive Delivery Systems: A Mini Review. *Drug Dev Ind Pharm* 30(10):1019–1028.

55. Arora S, Ali J, Ahuja A, Khar RK, Baboota S (2005) Floating drug delivery systems: A review. *AAPS PharmSciTech* 6(3):E372–E390.

56. Birnbaum DT, Brannon-Peppas L (2004) Microparticle Drug Delivery Systems. 117–135.

57. Loira-Pastoriza C, Todoroff J, Vanbever R (2014) Delivery strategies for sustained drug release in the lungs. *Adv Drug Deliv Rev* 75:81–91.

58. Stevenson CL, Santini JT, Langer R (2012) Reservoir-based drug delivery systems utilizing microtechnology. *Adv Drug Deliv Rev* 64(14):1590–602.

59. Bakh NA, et al. (2017) Glucose-responsive insulin by molecular and physical design. *Nat Chem* 9(10):937–943.

60. Sutradhar KB, Sumi CD (2016) Implantable microchip: the futuristic controlled drug delivery system. *Drug Deliv* 23(1):1–11.

61. Vegas AJ, et al. (2016) Combinatorial hydrogel library enables identification of materials that mitigate the foreign body response in primates. *Nat Biotechnol* 34(3):345–52.

62. Dhawan A (2015) Clinical human hepatocyte transplantation: Current status and challenges. *Liver Transplant* 21(S1):S39–S44.

Chapter 2: Vaccine kinetics

Overview

Subunit vaccines based on recombinant protein antigens combined with adjuvants can safely elicit protective humoral immune responses in humans, and they have become a cornerstone of modern public health (1, 2). Recent advances in structure-based vaccine design (3, 4) and progress in the development of adjuvants that are safe and effective for prophylactic vaccines (5) have helped drive the field. However, several challenges remain: A number of protein vaccines, such as candidate vaccines against HIV and malaria, have tended to elicit short-lived immunity (6, 7). In HIV, broadly neutralizing antibodies (BNAbs) isolated from infected patients are generally characterized by high degrees of somatic hypermutation (SHM) (8), but methods to generate such highly mutated antibodies by vaccination remain unknown. SHM occurs in germinal centers (GCs) within lymphoid organs, and data from animal models demonstrate a critical role for follicular helper T-cells in the induction of GCs and promotion of affinity maturation (9, 10). To date, methods to promote Tfh generation and long-lived germinal centers during vaccination remain unclear (11-15). Much attention has focused on the use of adjuvants to promote affinity maturation, but it remains unclear if adjuvants alone can provide the necessary immunological driving forces for promoting extensive affinity maturation (16). During acute infections, which often provoke robust germinal center responses and durable humoral immunity, microorganism replication typically occurs over the course of one to several weeks (17-19). During this time, recognition of molecular danger signals contained within the pathogen sustains stimulation of the innate immune system, and a continuous supply of antigen is provided to the adaptive immune system. In contrast to these patterns of antigen and inflammatory cues during infection, typical subunit vaccines

show much more rapid clearance following injection. During a primary immune response, parenterally-injected proteins are detected in lymph nodes within minutes to a few hours, but are largely flushed away within 1-2 days (12, 20). Adjuvants such as alum and MF59 are believed to act as antigen depots altering these kinetics, but biodistribution studies suggest that clearance of antigen from injection sites and lymph nodes is often nearly indistinguishable for soluble vs. alum-adsorbed or MF59-adjuvanted antigens (21-23). As such, the impact of subunit vaccine kinetics on the humoral immune response remains poorly understood. Given that germinal centers peak multiple weeks after antigen exposure, it is reasonable to postulate that antigen kinetics may have a profound impact on the magnitude and quality of the germinal center response and long-term humoral immunity.

Here we explored the effects of systematically varied temporal dosing patterns on the humoral immune response to model HIV subunit vaccines consisting of recombinant CD4 binding site-presenting gp120 monomer (24, 25) or SOSIP native-like HIV Env trimer proteins (26-28). We find that certain extended-duration dosing profiles increased the strength of the humoral response, with exponentially-increasing patterns providing the greatest enhancement. Guided by a computational model of the effects of vaccine kinetics on the germinal center response, we found that exponential-increasing dosing kinetics promoted capture and retention of the antigen in lymph nodes, leading to increased germinal center B-cell expansion, plasma cell generation, and Tfh cell numbers.

Exponentially-increasing dosing profiles during priming durably increase the production of antigen-specific IgG

We hypothesized that extended exposure to antigen and adjuvant, better mimicking the kinetics of live infections, would augment the response to vaccination. As a model vaccine, we employed a previously-described gp120 "stripped core" antigen containing the CD4 binding site (24, 25), which was mixed with monophosphoryl lipid A (MPLA) as a clinically-relevant adjuvant (29). We first evaluated the effect of altering vaccination kinetics by extending the dosing of the prime over 1 week. Groups of mice were immunized with either a conventional bolus injection on day 0, or 7 daily injections over 1 week testing three concepts: exponentially-increasing (exp-inc), exponentially-decreasing (exp-dec), or constant dosing, where the summed total dose of antigen and adjuvant was kept the same in all groups (Figure 2.1A and Table 2.1). All groups received a boost as a single bolus injection at day 21. Following priming, exp-inc and constant dosing profiles elicited strikingly higher IgG responses by day 14 compared to bolus immunization, with anti-gp120 Ab concentrations 14- and ~8-fold higher ($p < 0.001$) respectively than bolus injection at day 14, roughly equivalent to the titers achieved by traditional bolus immunization after the boost (Figure 2.1B-C). By contrast, an exp-dec dosing pattern elicited titers post-prime that were indistinguishable from the bolus control. Following the boost administered at day 21, animals that received an exp-inc prime continued to show higher anti-gp120 Ab levels, which were 2.7 times greater (average over time) than the bolus-primed group (Figure 2.1C, $p < 0.001$). This effect was durable, lasting 150 days. By contrast, the constant-dosing prime elicited Ab levels only 1.6 times higher than bolus injection ($p = 0.040$) and the exp-dec prime was not significantly

different from bolus prime. Thus, certain extended vaccine kinetic profiles, especially in an increasing dosing pattern, enhanced the long-term concentration of antigen-specific IgG produced.

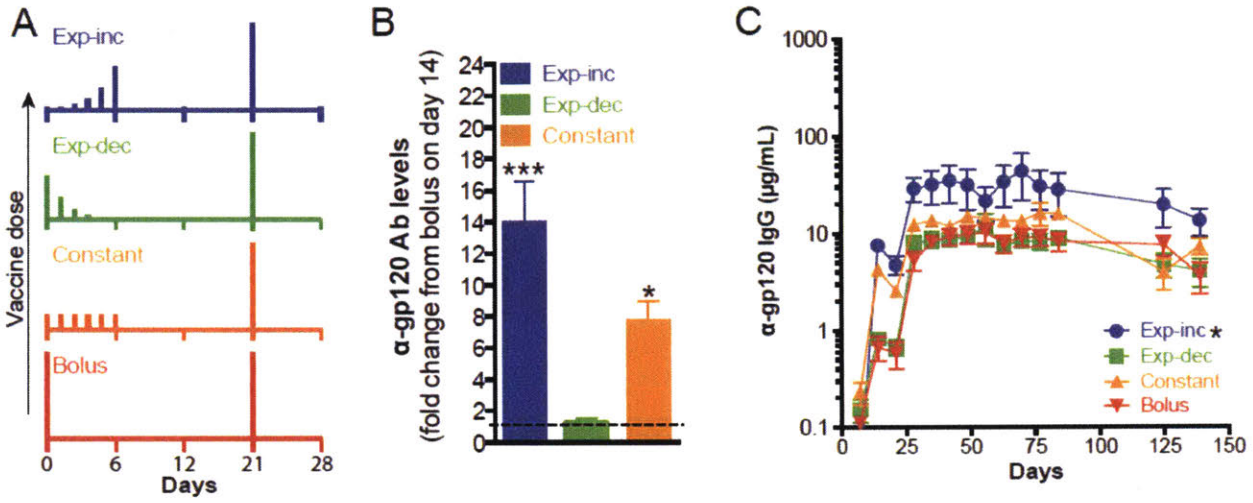

Figure 2.1. Exponentially-increasing dosing schedules during priming durably increase antigen-specific IgG production relative to traditional bolus immunization. Groups of C57BL/6 mice (n = 5/group) were immunized with 5 μg gp120 mixed with 25 μg MPLA according to the dosing schedules shown in (A), followed by a single bolus booster injection of 5 μg gp120 + 25 μg MPLA on day 21. (B) Fold change in antibody concentration on day 14 post-prime relative to bolus injection. *, p <0.05; ***, p <0.0001 compared to bolus injection determined by ANOVA with Dunnett's test *post hoc* using bolus injection as the control. Shown are means ± s.e.m. (C) Total serum anti-gp120 IgG as measured by ELISA. *, statistically different from boost d21 group as determined by 2-way ANOVA with Dunnett's *post hoc* test using bolus injection as the control. Data is representative of two independent experiments.

Table 2.1. Vaccine doses for each kinetic immunization pattern.

Dosing Profile:	Exponential increasing		Exponential decreasing		Constant		Bolus	
Day	gp120 (ug)	MPLA (ug)	gp120 (ug)	MPLA (ug)	gp120 (ug)	MPLA (ug)	gp120 (ug)	MPLA (ug)
0	0.010	0.050	3.089	15.446	0.714	3.571	5	25
1	0.026	0.130	1.188	5.941	0.714	3.571	-	-
2	0.068	0.338	0.457	2.285	0.714	3.571	-	-
3	0.176	0.879	0.176	0.879	0.714	3.571	-	-
4	0.457	2.285	0.068	0.338	0.714	3.571	-	-
5	1.188	5.941	0.026	0.130	0.714	3.571	-	-
6	3.089	15.446	0.010	0.050	0.714	3.571	-	-

Extended dosing profiles over two weeks maximize antibody titers

We hypothesized that dosing over a 1 week period may be suboptimal, given the more prolonged kinetics of germinal centers and the kinetics of many acute infections. As exp-inc dosing resulted in elevated antibody titers, we next tested how the duration of this dosing pattern influenced the humoral response. We compared exp-inc dosing profiles administered over 7, 14, or 21 days, keeping the total number of injections (7) and total dose constant. For each pattern, the bolus boost was given 14 days after the last priming injection (Figure 2.2A and Figure 2.3A). In order to account for the effect of a later boost, we also introduced a second control with single dose prime and a boost at day 28. As seen in Figure 2.2B, extending the dosing course from 7 to 14 days increased the magnitude of the antibody response, with the 2-week exp-inc dosing pattern eliciting ~48-fold higher concentrations of gp120-specific antibodies than the corresponding bolus

prime group by day 21 ($p < 0.001$, Figure 2.2B). Further extending the exp-inc dosing profile from 14 days to 21 days led to a slightly weaker humoral response than the 2-week profile (Figure 2.3). Post-boost, 1-week and 2-week exp-inc dosing elicited sustained gp120-specific IgG levels that were 3.6-fold ($p < 0.001$) and 6.6-fold higher ($p < 0.001$)

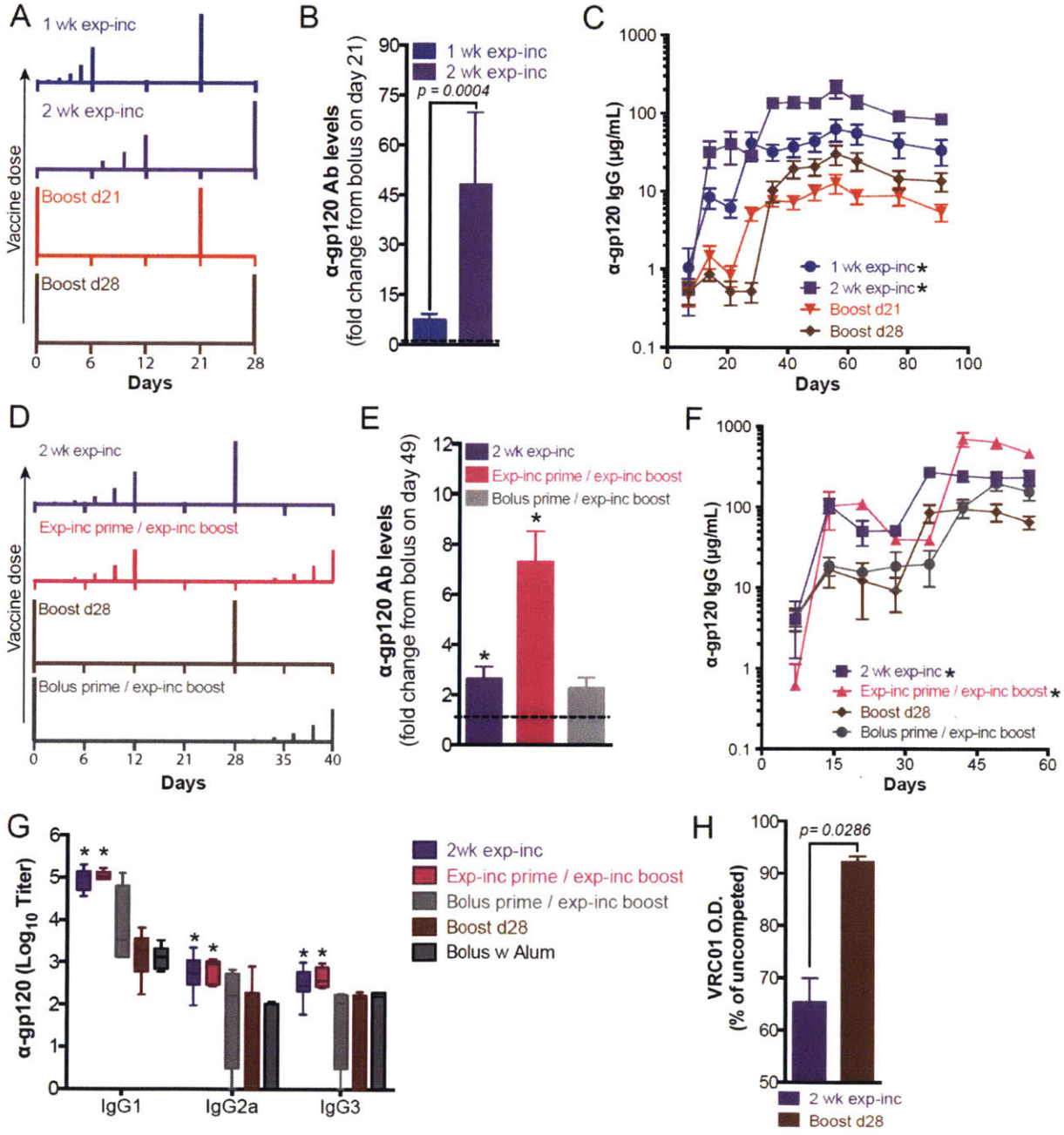

than their equivalently-timed bolus prime/boost controls (Figure 2.2C).

Figure 2.2 Exponentially-increasing dosing profiles extended over 2 weeks with an exponentially-increasing boost enhance the humoral response.
Groups of C57BL/6 mice were immunized with 5 μg gp120 + 25 μg MPLA following the dosing schedules shown in (A) and (D). (B) Fold change in antibody concentration on day 21 post-prime relative to bolus injection. *p* was determined by unpaired Mann-Whitney test. (C) Total serum anti-gp120 IgG (n = 10/group) as measured by ELISA. *, statistically different from boost d21 group as determined by 2-way ANOVA with Dunnett's *post-hoc* test using bolus injection as the control. (E) Fold change in antibody concentration on day 49 (post-boost) relative to bolus injection. *, p <0.05 determined by Kruskal-Wallis test with Dunn's multiple comparison's test. (F) Total serum IgG (n = 5/group) measured by ELISA. *, statistically different from boost d21 group as determined by 2-way ANOVA with Dunnett's *post-hoc* test using bolus injection as the control. (G) Mice were immunized either with gp120 plus MPLA following schedules shown in (D) or with gp120 formulated in 100 μg alum (aluminum phosphate, prime day 0, boost day 28). Serum was collected at day 49 and anti-gp120 isotype titers were analyzed by ELISA. *, statistically different from boost d28 group as determined by 2-way ANOVA with Dunnett's *post-hoc* test using bolus injection as the control. (H) ELISA for binding to gp120 for day 49 sera was performed in the presence of competing broadly-neutralizing antibody VRC01. Shown is ELISA optical density as a percentage of uncompeted signal. *p* was calculated by unpaired Mann-Whitney test. All values shown are mean ± s.e.m. Data are representative of experiments done twice (A-C) or once (D-H), using at least 5 mice per group.

To determine the relative importance of an increasing dosing profile on the prime vs. boost response, we compared exp-inc dosing profiles administered only during the prime, only during the boost, or during both prime and boost (Figure 2.2D). Incorporation of an exp-inc dosing profile for both the prime and boost resulted in significantly higher serum Ab concentrations than either exp-inc prime/bolus boost or bolus prime/exp-inc boost regimens (Figure 2.2E-F). To evaluate the impact of extended dosing on class switching, we analyzed titers of different Ab isotypes induced. Exp-inc dosing substantially increased the titers of multiple Ig isotypes, including IgG1, IgG3, and IgG2a that was near background following traditional bolus immunization (Figure 2.2G). We also compared exp-inc vaccination to traditional bolus vaccination using alum as the most common clinical adjuvant, which has been proposed to provide a depot effect with some antigens

(30). As shown in Figure 2.4, alum provided comparable antibody responses to bolus vaccination using MPLA as adjuvant (p = 0.88), but was much inferior to exp-inc dosing of the vaccine, and also elicited almost exclusively IgG1 titers (p = 0.038, Figure 2.2G). Finally, we tested the capacity of vaccine-elicited antibodies to compete with the BNAb VRC01 for binding to the gp120 antigen by ELISA, exp-inc vaccine dosing increased the proportion of antibodies induced that blocked VRC01 binding (Figure 2.2H).

Altogether, these results indicate that for a given total quantity of antigen and adjuvant, extended vaccine kinetics obtained by administering the vaccine over at least 2 weeks in increasing doses is capable of durably increasing total output serum concentrations of elicited antigen-specific IgG by more than 7-fold, elevating the production of multiple isotypes of Ab.

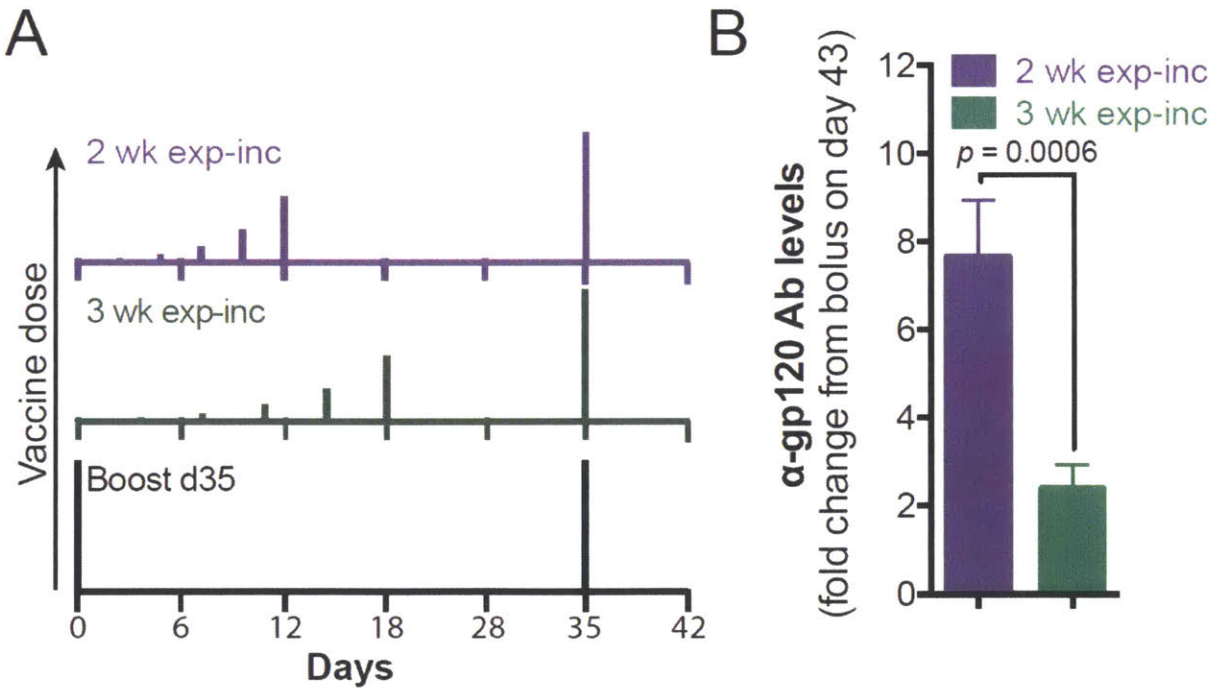

Figure 2.3. Extending exponential increasing dosing over 3 weeks results in lower antibody titers.
Groups of C57BL/6 mice (n = 5/group) were immunized with 5 μg gp120 + 25 μg MPLA following the dosing schedules shown in (A). (B) Fold change in antibody concentration on day 43 (post-boost) relative to bolus prime and boost injections. p value determined

by unpaired Mann-Whitney test. Data is representative of two independent experiments, using 5 mice per group.

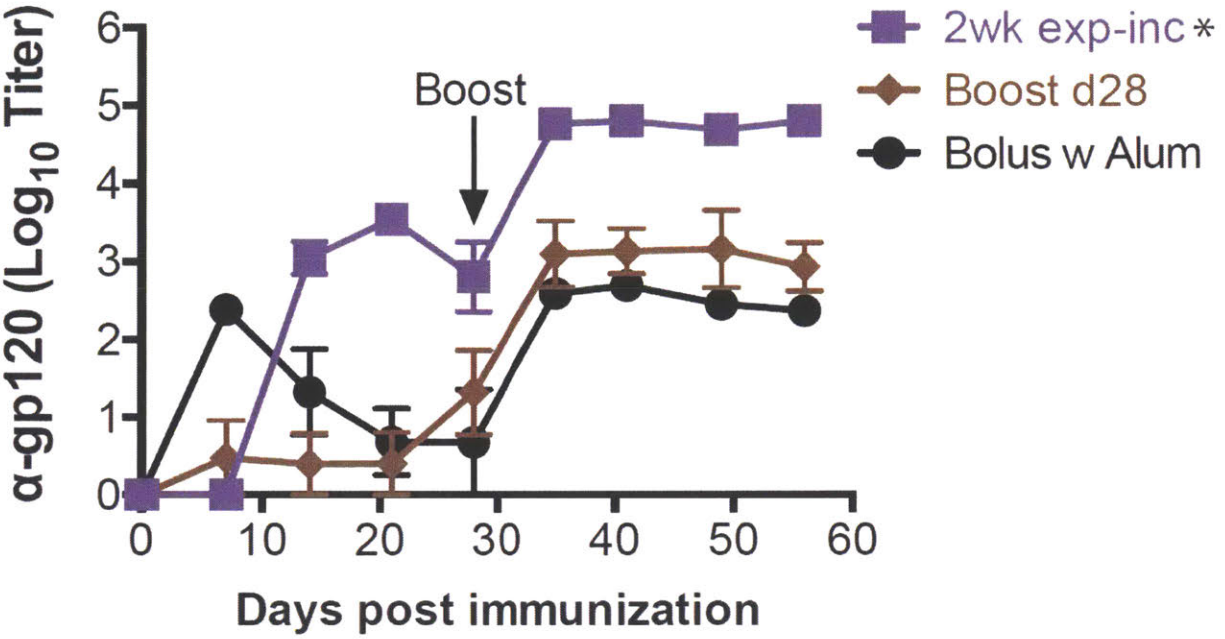

Figure 2.4. Exp-inc vaccine dosing elicits substantially higher antibody titers than vaccination with alum.
Groups of C57BL/6 mice (n = 5/group) were immunized with 5 μg gp120 + 25 μg MPLA following the dosing schedules shown in Fig. 2D. The alum group received bolus immunization with 5 μg gp120 and 50 μg alum (aluminum phosphate) following the same schedule as the bolus "Boost d28". Shown are serum gp120-specific IgG titers vs. time. *, statistically different from boost d28 group as determined by 2-way ANOVA with Dunnett's post-hoc test using bolus injection as the control.

A computational model of the germinal center response predicts antibody-based feedback governs the response to extended dosing vaccines

In a traditional bolus immunization, the half-life of the antigen present in lymph nodes is shorter than the time scale over which germinal center (GC) reactions start producing higher affinity IgG antibodies relative to the initial IgM response (12, 20). Thus, most antigen displayed on follicular dendritic cells (FDCs) is in the form of immune complexes (IC) of antigen with weakly-bound IgM antibodies (31, 32); this may lead to a sub-optimal

level of antigen concentration on FDCs. We hypothesized that extended vaccine dosing may better match the timescale of antigen availability to the kinetics of the GC reaction compared to bolus immunization, leading to more ICs formed with newly-evolved higher affinity antibodies, thereby promoting more prolonged retention on FDCs. To explore whether this feedback mechanism alone can account for the significant effect of extended dosing profiles observed experimentally, we constructed a coarse-grained computational model with a minimal number of parameters. The goal of the model was to test whether our hypothesis could provide an explanation for the data, and if so, to subject it to experimental tests. The model particularly focuses on antigen transport, the germinal center (GC) reaction, and antibody production by plasma cells in a lymph node (Figure 2.5A). It makes the following assumptions: (1) As a simplified approximation of experimental observations of soluble antigen transport following injection, we assume that antigen arrives at the lymph node immediately following immunization, and free antigen in the lymph node clears exponentially over time with a half-life of approximately 17 hr (20, 33). Natural IgM initiates the immune response and captures antigen arriving in the lymph node with a low affinity (32). (2) B-cells class-switch only to IgG and not to other Ig subclasses after the GC reaction ensues. (3) The onset of IgG production occurs 6 days after the initial antigen injection, reflecting the observation that it takes a few days for GC reactions to occur before class switching initiates (34, 35). (4) The GC B-cell population size is assumed to be constant during the GC reaction. While this is incorrect, qualitative results emerging from models of evolutionary processes that make this approximation are often accurate (36). (5) The formation of immune complexes (ICs) is the rate-limiting step in antigen presentation to GC B-cells; i.e., the model assumes that transport of immune

complexes to FDCs is relatively fast. (6) 10% of selected B cells differentiate to plasma cells (24). (7) IgG affinity evolves linearly, and increases by 100-fold by the end of the GC reaction (24). Based on these assumptions, four key reactions summarize the model (Figure 2.5B). During the early phase of the immune response, free antigen is captured by IgM at a slow rate (proxy for affinity), β_1 (Figure 2.5B, Reaction 1). B-cells bind to ICs in GCs with an increasing rate β_2 (proxy for affinity) as a function of time, and become plasma cells (Figure 2.5B, Reaction 2), which ultimately leads to production of IgG (Figure 2.5B, Reaction 3). Because this is a coarse-grained model, we consider only the average affinity of IgGs, although in reality there is a heterogeneous distribution. Plasma cells derived from the GC reaction produce antibodies at a rate k (Figure 2.5B, Reaction 3), and the resulting higher affinity antibodies capture antigen (Figure 2.5B, Reaction 4) at a rate β_2. Parameter values were taken from the literature (Table 2.2) when available, except for k, which is the number of antibodies produced by each plasma cell per day. Non-linear regression fitting of the model antibody output to IgG concentrations measured experimentally at days 7 and 14 following gp120 immunizations was performed to determine the best value of k. This yielded a value for k of 2.56×10^6 antibodies per plasma cell per day, which in rough agreement with the reported rate of $\sim 10^7$ IgG molecules secreted by a single plasma cell per day (37).

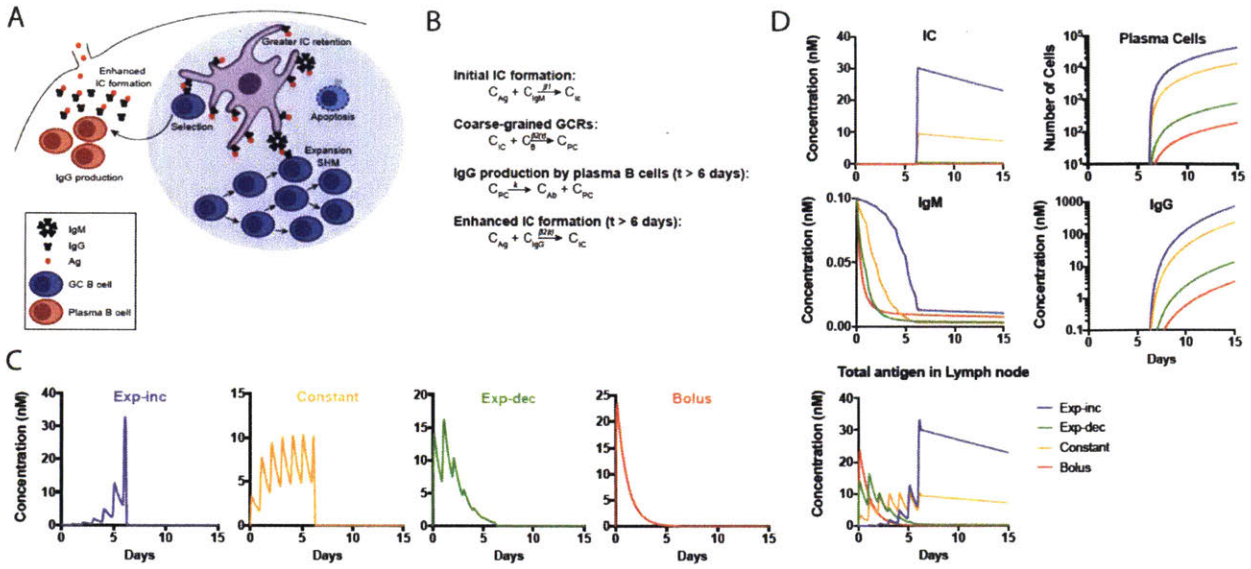

Figure 2.5. A computational model of the germinal center response predicts enhanced immune complex formation and IgG production by extended-dosing/increasing vaccination profiles.

(A) Schematic of components of antigen transport, GC reaction and antibody production model. (B) Four reactions of the model including antigen capture by ICs at initial and later stages of the immune response, coarse-grained germinal center reaction and antibody production. C_B, concentration of germinal center B cells; C_{Ag}, concentration of free Ag; C_{IC}, concentration of ICs; C_{IgM}, concentration of IgM; C_{IgG}, concentration of IgG; C_{PC}, concentration of plasma cells. (C) Kinetic profile of free antigen in lymph nodes predicted by the model with fitted *k*. ($2.56 * 10^6$ antibodies/plasma cell per day) (D) Kinetic profiles of IC, IgM, IgG, Plasma cells and Total antigen in lymph node (free Ag+ IC) predicted by the model. See also Germinal center model calculations in Materials and Methods and Equation S1. for mathematical representation of the model.

Table 2.2. Parameter values and initial conditions used in the model.

Parameter	Value	Reference
D_{Ag}, Free antigen decay rate	1/day	61
D_{Ab}, IgG decay rate	0.0233/day	62
D_{IC}, FDC presented IC decay rate	0.0233/day	63
D_{PC}, Plasma cell death rate	0.03/day	63
β1, Basal level on-rate	10^3/(M*S)	64
γ, GCB cell concentration	$1.44x10^{-12}$ M $(= \frac{10^4 Bcells}{GC}\,{}^{1}X\,\frac{100GCs}{lymph\_node}\,{}^{2}X\,\frac{1mol}{6.02x10^{23} cells}\,X\,\frac{1}{1uL}\,{}^{3})$	1. 65 2. 66 3. 67
Initial conditions	**Value**	**Reference**
$C_{Ag}(t=0)$, $C_{IC}(t=0)$, $C_{IgM}(t=0)$, $C_{IgG}(t=0)$, $C_{PC}(t=0)$	$[0,0,10^{-10},0,0]$	68 Initial concentration of natural IgM was taken to be proportional to the level of IgG measured at day 7 multiplied by the ratio of IgG/IgM binding to SAg-gp120 (1:1) before immunization, to reflect the IgM level before immunization

Using these parameters, we modeled the GC reaction, immune complex formation, and IgG production for each of the 1-week vaccine dosing schedules studied experimentally in Figure 2.1 (Figure 2.5C). As shown in Figure 2.5D, the model predicts that the hierarchy of antibody production among the different dosing schemes mirrors the hierarchy of IC concentrations. Exp-inc dosing produces the highest level of immune complex formation and thus the highest level of antibody output. The exp-inc dosing profile also leads to increased GC activity and increased numbers of plasma cells. By contrast, the calculations suggest that IC accumulation using the exp-dec dosing scheme is very low and similar to that from a bolus immunization (Figure 2.5D), consistent with the experimental finding that antibody production in these two cases was similar. A key

prediction of the model is that total antigen in lymph nodes quickly decays 24 hr after the bolus immunization, while antigen is retained at high levels for many days at the end of the exp-inc dosing schedule (Figure 2.5D). Thus, a simple model of the GC reaction focused on the impact of early antibody evolution on antigen capture in ICs reproduces the qualitative results seen in our experiments, and suggests that a key mechanism of action is enhanced capture/retention of antigen in lymph nodes in the exp-inc dosing profiles.

Exponential-increasing dosing results in prolonged antigen retention in lymph nodes and enhanced germinal center formation

Motivated by the modeling predictions, we performed a series of experiments using infrared dye-labeled gp120 to track the amount of antigen retained in draining lymph nodes over time, and evaluated GC induction following priming with bolus immunization or exponentially-increasing dosing. Groups of mice were immunized with labeled gp120 and MPLA, then serially sacrificed to recover tissues for digestion and quantification of total gp120 fluorescence in the draining inguinal LNs at selected time points. Lymph nodes were analyzed at 24 and 72 hr following bolus injection, or 24 and 72 hr after the final injection in a 2-week exp-inc dosing regimen Figure 2.6A). Following bolus immunization, antigen was detected in the LNs at 24 hr, but quickly decayed thereafter (Figure 2.6B). By contrast, at the end of the exp-inc dosing regimen, antigen remained at high, approximately constant levels for at least 3 days. To determine the anatomical localization of retained antigen, we repeated this experiment using phycoerythrin (PE) as an intrinsically fluorescent model protein antigen, vaccinating with a bolus or exp-inc

dosing regimen. Twenty-four hr after bolus immunization, little or no antigen could be detected on FDCs or any other location in lymph nodes, while 24 hr after the final injection in the exp-inc regimen, substantial amounts of PE were detected lining the FDC network (Figure 2.6C). Thus, exp-inc dosing enhanced antigen retention in lymph nodes at the end of the injection schedule compared to bolus vaccination, with preferential retention on FDCs, as predicted by the computational model of the GC reaction.

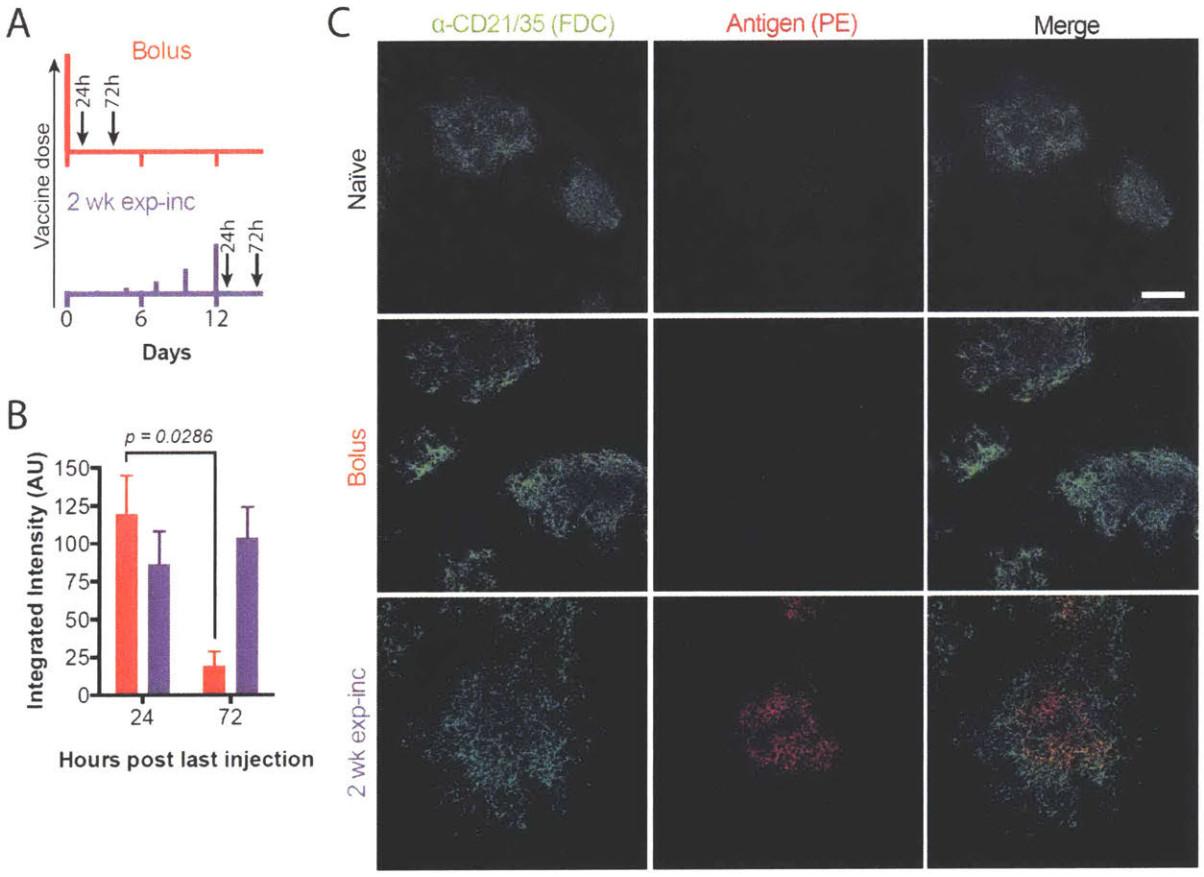

Figure 2.6. Exponential-increasing vaccine dosing leads to enhanced antigen capture and retention in draining lymph nodes.
Groups of albino C57BL/6 mice received s.c. injections of 5 μg of IRDye800-labeled gp120 plus 25 μg of MPLA. Relative amounts of gp120 in the lymph nodes were quantified by fluorescence. (A) Dosing and sampling profiles used in this experiment. (B) Fluorescence detected from lymph nodes *ex vivo* (n = 4/group) at 24 or 72 hours post last injection. p value was calculated by unpaired Mann-Whitney test. Data is representative of two independent experiments. (C) Groups of C57Bl/6 mice (n=2/group) were vaccinated with 5 μg phycoerythrin and 25 μg MPLA by bolus or exp-

inc dosing following the schedule in (A), followed by collection of lymph nodes for imaging at 72 hr after bolus or after last injection of 2wk exp-inc dosing. FDC networks were labeled *in situ* by i.p. injection of anti-CD21/35 antibody 16 h prior to tissue collection. Collected tissues were clarified and imaged intact by confocal microscopy; shown are maximum intensity projections from z-stacks through FDC clusters. Scale bar 80 μm.

We next analyzed B-cell populations in the draining inguinal lymph nodes of mice receiving bolus vs. 2-week exp-inc vaccine dosing regimens (Figure 2.7A). Germinal center B-cells were tracked over time, and plasmablasts were compared by flow cytometry on days 7 and 13 for both regimens. Significant numbers of GC B-cells did not develop following bolus immunization until day 13 and the GCs contracted by day 21 (Figure 2.7B-C). Exp-inc-vaccinated mice showed germinal center responses over a similar timeframe, but GC B-cell numbers escalated dramatically between day 7 and 13, reaching 3.7-fold higher peak levels of GC B-cells ($p = 0.040$ for 2wk exp-inc d13 vs Bolus d13, Figure 2.7B-C). Notably, exponential dosing led to overall greatly increased cell numbers in lymph nodes at these peak GC time points. Adjuvant-only and antigen-only controls indicated that this germinal center response was largely antigen-specific but dependent on the presence of adjuvant (Figure 2.7C). Exp-inc vaccination also stimulated a massive expansion of plasma cells on day 13, which was not observed at any time point for traditional bolus immunization ($p < 0.0001$, Figure 2.7D). B-cell activation in the draining LNs at 24 hr after the final injection of the exp-inc dosing regimen was similar to 24 hr post bolus injection (Figure 2.7E). Thus, an escalating pattern of vaccine dosing amplified the germinal center response and altered B-cell differentiation patterns in the lymph node.

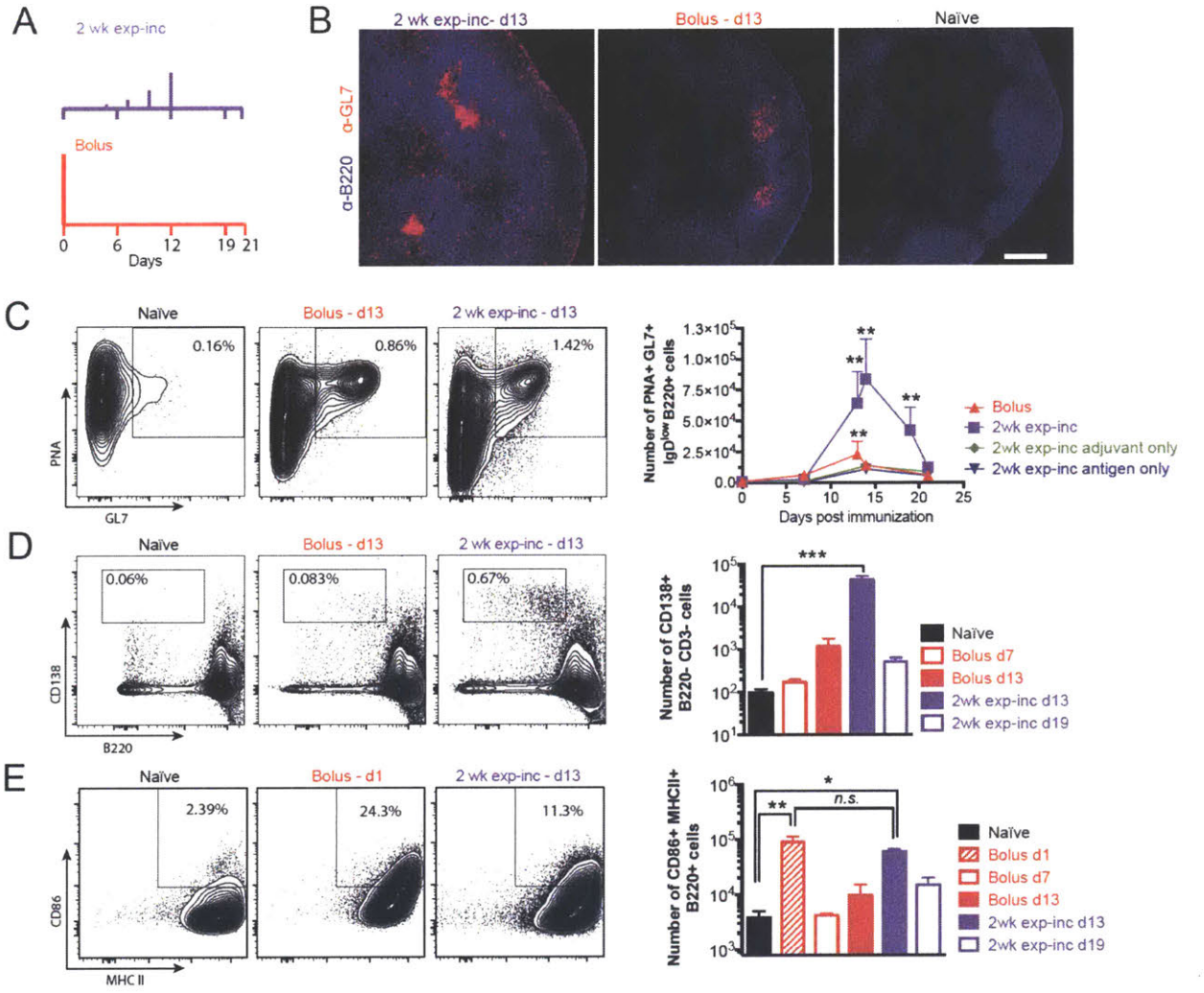

Figure 2.7. Exponential-increasing vaccine dosing promotes germinal center B-cell differentiation.

C57BL/6 mice were immunized with either 5 μg gp120 and 25 μg MPLA, MPLA only or gp120 only, following the dosing schemes depicted in (A). (B) Lymph node sections were stained for B-cells (B220, blue) and GL7 (pink), and analyzed by confocal microscopy (10x magnification). (C-E) Draining LNs were collected at the indicated time points, and cell suspensions were analyzed by flow cytometry to detect germinal center B cells (C, $GL7^{+}PNA^{+}IgD^{low}$), plasmablasts (D, $CD138^{+}B220^{-}$) and activated B cells (E, $B220^{+}MHCII^{+}CD86^{+}$). Representative flow cytometry plots (left) and cell counts (right) are shown. *, $p < 0.05$; **, $p < 0.01$, ***, $p < 0.001$ determined by Kruskal-Wallis test with Dunn's multiple comparison's test. Error bars are s.e.m. Data is representative of four independent experiments.

True continuous antigen exposure elicits increased germinal center and serum antibody responses

Because we experimentally prolonged vaccine dosing through repeated injections, a question that remained was whether similar vaccine results would be obtained in the setting of true continuous antigen exposure. To answer this question, a series of experiments were performed using mini osmotic pumps, non-mechanical delivery devices that can release a material continuously over a specific period of weeks *in vivo* when implanted subcutaneously. Mice were immunized with osmotic pumps containing native-like BG505 SOSIP HIV Env trimers (26-28) admixed with an ISCOMs-type adjuvant, and $CD4^+$ T-cell, B-cell, and antibody responses were assessed. As shown in Figure 2.8A, we compared traditional bolus vaccination with SOSIP trimer and ISCOMATRIX to immunizations where osmotic pumps were implanted for release of vaccine over 1 week, or immunizations using pumps releasing vaccine for 2 weeks. Motivated by our results that suggest the key feature of the escalating dosing pattern is the availability of antigen at the end of the dosing schedule, we administered a bolus injection at the end of each pump lifespan (day 7 and day 14, for the 1 week and 2 week pumps, respectively) to provide a high dose of antigen at the end of the dosing pattern. Animals in each group were boosted with the same regimens after 8 weeks and 19 weeks. We evaluated GC B-cell and Tfh cell numbers 4 weeks after the final immunization. Sustained immunogen delivery using the osmotic pumps increased the frequency and absolute number of germinal center Tfh cells ($CXCR5^{hi}$ $PD\text{-}1^{hi}$, Figure 2.8B) and overall Tfh cells (Figure 2.8C) in the draining lymph nodes. The greatest GC Tfh increase (~3 fold) was observed for pumps providing 2 weeks of vaccine release. Total numbers of Tfh cells ($CXCR5^+BTLA^{hi}$)

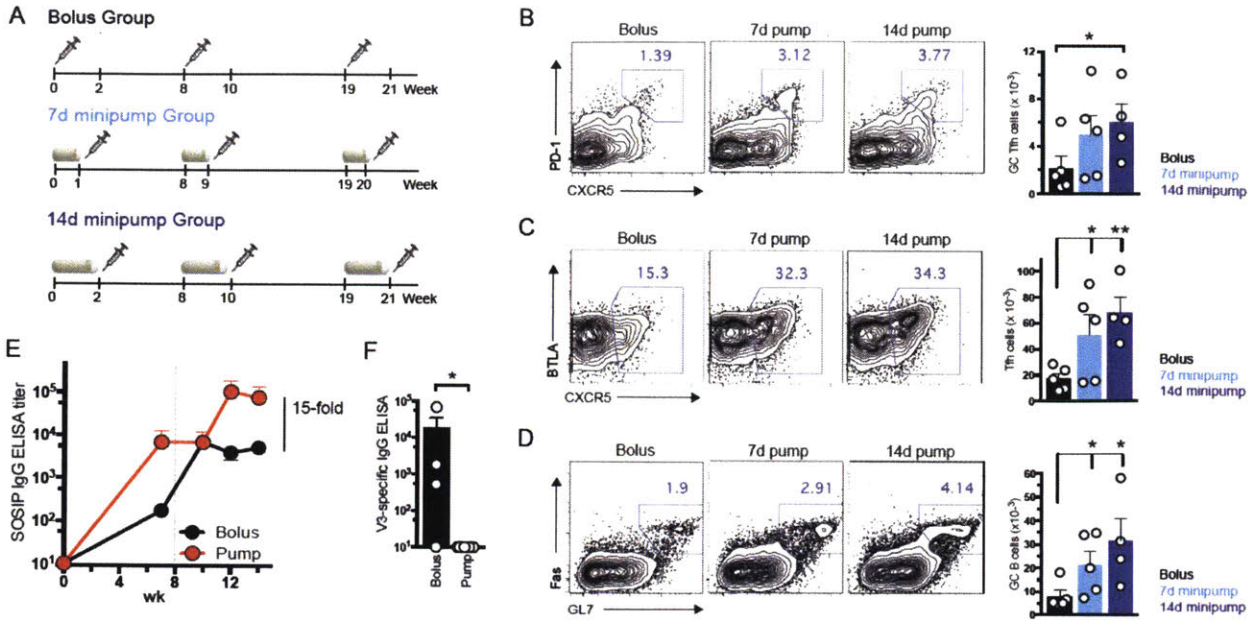

Figure 2.8. Continuous vaccine release via osmotic minipumps leads to increased Tfh and GC B cells and amplified antibody responses.
(A-D) C57BL/6 mice were immunized with 20μg HIV-1 Env BG505 SOSIP trimer via conventional bolus injection, 'Bolus'. A second group, '7d minipump', was immunized with 7-day minipumps continuously releasing HIV-1 Env BG505 SOSIP trimers (50 μg, 7.1 μg/day), supplemented with 20 μg BG505 SOSIP trimer via bolus injection at the end of each 7d pump immunization. A third group, '14d minipump', was immunized with 14-day minipumps continuously releasing HIV-1 Env BG505 SOSIP trimers (100 μg, 7.1 μg/day), supplemented with 20μg BG505 SOSIP trimer via bolus injection at the end of each 7d pump immunization. A course of three immunizations was used, paralleling a human vaccine schedule. (B-D) Draining LNs were collected at wk 24, four weeks after the final immunization, and lymphocytes were analyzed by flow cytometry to detected (B) GC Tfh cells ($CXCR5^{+}PD\text{-}1^{hi}$), (C) Tfh cells ($CXCR5^{+}BTLA^{hi}$), and (D) germinal center B cells ($FAS^{hi}GL7^{hi}$). Representative flow cytometry plots (left) and cell counts (right) are shown. (E-F) B6 mice were immunized with conventional 20μg bolus injections of HIV-1 Env BG505 SOSIP trimers ('Bolus'). A second group was immunized with 14-day minipumps continuously releasing HIV-1 Env BG505 SOSIP trimers (1.4 μg/day), supplemented with 20 μg BG505 SOSIP trimer via bolus injection at the end of the 14d pump immunization ('pump'). ISCOMATRIX adjuvant was used in each case. (E) Env trimer binding IgG was quantified by ELISA. Dotted line indicates time of second immunization (wk8). (F) ELISA for off-target V3 loop antibodies. Data are representative of two independent experiments. *, $p < 0.05$; **, $p < 0.01$. Error bars are s.e.m.

measured by flow cytometry were also increased by osmotic pump-based sustained vaccine kinetics, with 2 week osmotic pumps eliciting the greatest increase in total Tfh numbers compared to bolus immunizations (Figure 2.8C). Overall numbers of GC B-cells

were elevated ~3-fold by the 2-week extended dosing osmotic pump regimen (Figure 2.8D), consistent with the knowledge that GC B cell numbers closely correlate with the availability of GC Tfh cells. No response was observed in animals receiving adjuvant alone (Figure 2.9).

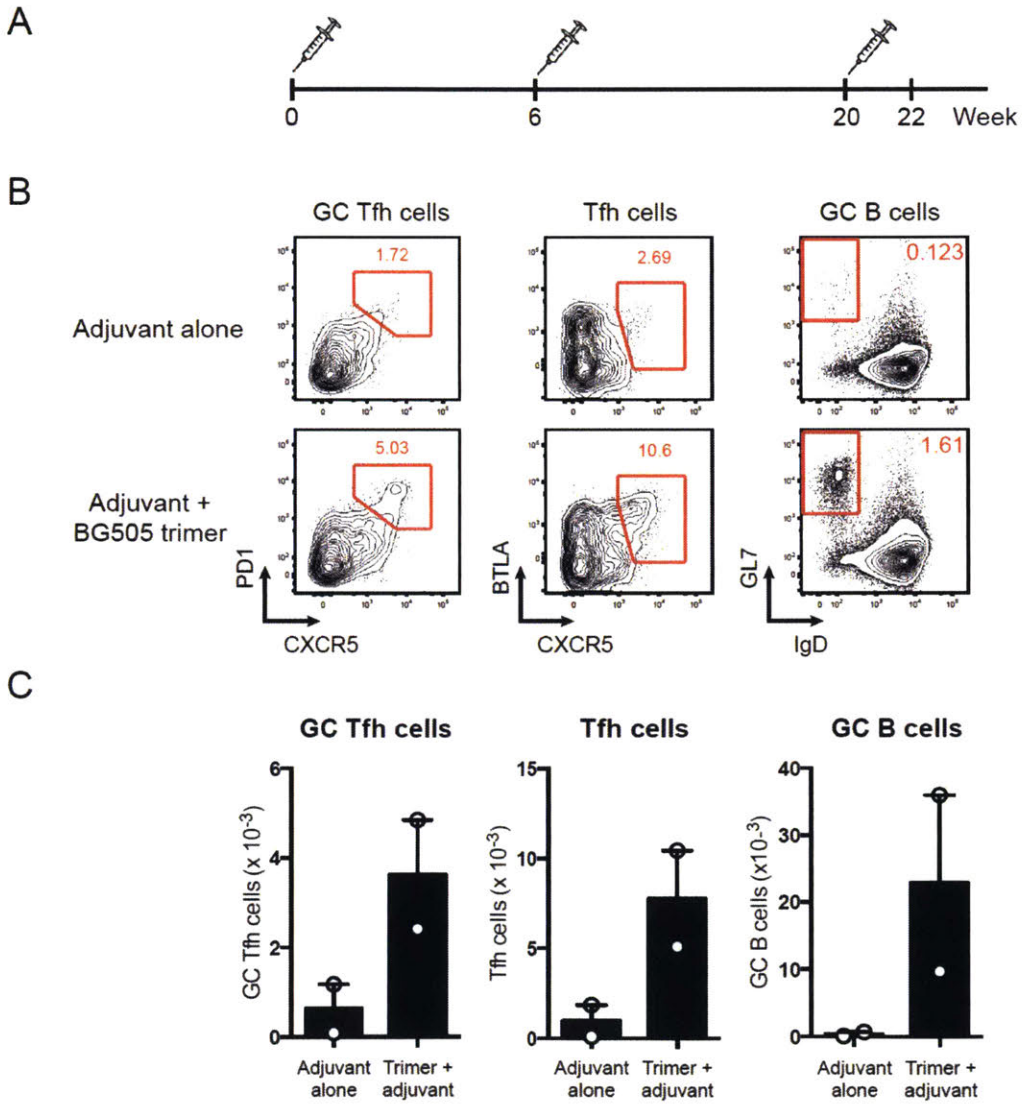

Figure 2.9. Adjuvant alone does not induce germinal center responses.
(A) C57BL/6 mice were immunized with 0.2 μg ISCOMs alone or with 10 μg BG505 SOSIP trimers and 0.2 μg ISCOMs at Weeks 0, 6, and 20. Germinal center responses in draining lymph nodes were analyzed at Week 22. (B) Flow plots and (C) graphs of GC Tfh cells ($CXCR5^{+}PD\text{-}1^{hi}$), Tfh cells ($CXCR5^{+}BTLA^{hi}$), and germinal center B cells ($FAS^{hi}GL7^{hi}$) in draining lymph nodes of mice immunized with adjuvant alone or with trimer and adjuvant.

Native-like SOSIP Env trimers generally elicit very low serum antibody responses after primary immunization (38, 39), which is a common feature of many protein immunogens. In contrast, provision of immunogen by extended *in vivo* release elicited significant anti-trimer IgG responses after the first immunization (Figure 2.8E). These enhancements translated to a 15-fold increase in total SOSIP-specific IgG titers in the serum after booster immunization (P=0.0062, Figure 2.8E). Additionally, consistent with our previous study (39), bolus immunization led to a preponderance of antibodies directed against the V3 loop not exposed on the intact trimer, suggesting some degree of active degradation of the immunogen *in vivo* (Figure 2.8F). These non-neutralizing V3-specific responses were not detected in the osmotic pump-immunized animals (Figure 2.8F), demonstrating that the osmotic pumps both provide robust immunological response benefits by altering the antigen dose kinetics and protect the immunogen structure. Thus, consistent with our findings from dosing profiles achieved by repeated injections, extended vaccine dosing with osmotic pumps led to increased antibody titers and GC development.

Discussion

The majority of licensed vaccines are thought to protect through the induction of long-lived neutralizing antibody responses (40). Methods to enhance humoral immunity and particularly to promote the germinal center reaction where antibody affinity maturation occurs are of great interest for improved vaccines, and may be especially important for the development of a successful HIV vaccine (41-43). Strategies to influence the B-cell response include the selection of appropriate adjuvants (5), use of multiple immunogens

to "steer" antibody responses (44, 45), and control over the dose and timing of antigen and adjuvant exposure through the method of vaccine delivery (46). Recent unexpected findings with HIV Env protein vaccines in non-human primates demonstrating that a variety of clinically-relevant adjuvants fail to promote affinity maturation to degrees greater than injection of protein alone indicate that adjuvants alone may not be capable of inducing optimal antibody responses (16).

Here we focused on the temporal profile of vaccination and its impact on the humoral response. Generating three basic temporal patterns of vaccine exposure, we found that administering antigen in increasing doses with time led to humoral responses that were significantly greater than constant-dosing or decaying-dosing profiles. Exponential-increasing dosing over 2 weeks at both prime and boost durably increased antibody titers 19-fold relative to traditional bolus immunizations. A computational model suggested that extended antigen dosing profiles lead to better antigen capture in the germinal center because of the delayed nature of IgG IC formation. These predictions were borne out by experimental analyses demonstrating that exponential-increasing vaccine kinetics led to prolonged antigen retention in lymph nodes and enhanced germinal center induction.

A number of studies have sought to enhance immune responses through the use of controlled-release devices to sustain vaccine exposure over prolonged periods, but these efforts have largely focused on the notion of replacing repeated injections with constant continuous exposure over 1 or more months, and mechanisms underlying the response to such sustained release formulations have not been explored (47-50). We were inspired by the previous work of Johansen et al. (51), who demonstrated that T-cell responses to peptide vaccination are substantially enhanced by immunizing in an increasing dosing

pattern. Here we show that such vaccine kinetics are also highly favorable for the antibody response, through the interplay of antibody production and B-cell stimulation in germinal centers. The strong influence of vaccine kinetics on the antibody response is likely an evolved mechanism optimizing B-cell activation in the face of replicating pathogens. Antigen load and inflammation during acute infections follow similar kinetic patterns as the exponential-increasing dosages that elicited optimal antibody titers and GC induction in these simple protein vaccinations. Furthermore, GCs can be active for weeks or months, and thus it is logical that the availability of vaccine antigen at later time points in that process can be an important limiting factor for the quantity and quality of the memory B cells and plasma cells produced by the GCs.

Though we focused our studies here on fixed doses of antigen/adjuvant, the total dose of the vaccine will also play an important role in the immunization outcome; for example, too high a level of antigen will cause the development of low affinity antibodies. While we found that an increasing antigen dosing profile can produce higher antibody titers, two important questions were not answered: 1) What is the dosing kinetic scheme that also leads to high affinity antibodies, not just higher titers? 2) Are there dosing kinetic schemes that are even more efficient than the exponentially increasing scheme that we studied? The possibility of an optimal dosing profile is suggested by the fact that intermediate antigen concentrations lead to the highest affinity antibodies (24) and that an optimal dosing profile may be one that matches the kinetics of dosing with the natural time scales of the GC reaction. Answering these questions will require that a large parameter space of dosing intervals and kinetic patterns be explored. Future studies are also needed to

determine whether these profiles increase the rate of somatic hypermutation, which is known to be important in HIV protection.

For widespread prophylactic vaccines meant for global distribution, it is impractical to envision vaccine regimens based on a daily series of injections, especially in the developing world where access to healthcare system can be challenging. Thus, an important next step for the concepts presented here will be implementation of vaccine delivery methods that allow vaccine exposure patterns as described here to be achieved following a single administration. Methods that may be suitable include the use of microneedle patches, biodegradable microparticles, or other controlled-release devices (52-55). Such delivery systems have been shown to be able to deliver large proteins and other vaccine components in increasing dose profiles. They are also well-characterized, have in some cases been commercialized, and their release kinetics are generally well understood (56, 57).

In summary, we have demonstrated that prolonged vaccine exposure during germinal center induction leads to enhanced GC B-cell differentiation and antigen-specific antibody production. Computational modeling suggested this effect was driven by enhanced capture of antigen in lymph nodes by evolving higher-affinity antibodies early in the GC response, a prediction borne out by experimental measurements of antigen retention in lymph nodes. To our knowledge, this work is the first to demonstrate a key role for vaccine kinetics in the response of B cells to immunization, and may prove to be an effective method for increasing the efficacy of subunit vaccines.

Materials and Methods

Materials

His-tagged Gp120 was expressed in HEK293 cells in serum-free media for one week and the supernatant was purified with Talon metal affinity chromatography resin (Clontech) followed by size-exclusion chromatography. The plasmid used was from Mata-Fink et al (25). BG505 SOSIP.664 trimers were expressed in HEK293 cells expressing the SV40 large T-antigen (HEK293T) or Chinese hamster ovary (CHO) cells and purified with a 2G12 mAb-affinity column followed by size-exclusion chromatography as previously reported (28, 58). Poly-L-Lysine hydrobromide (MW 500-2000) and monophosphoryl lipid A (MPLA) from *Salmonella enterica* serotype Minnesota Re 595 were purchased from Sigma-Aldrich. Bovine serum albumin (BSA; IgG-free) and HRP-conjugated goat anti-mouse IgG, Fc fragment specific (HRP-IgG) were purchased from Jackson ImmunoResearch. IRDye 800CW-NHS was purchased from LI-COR Biosciences. HRP-conjugated goat anti-human IgG and Fc fragment-specific (HRP-IgG) Anti-human HRP-IgG were purchased from Fisher Scientific. 3,3',5,5'-Tetramethylbenzidine (TMB) was purchased from eBioscience.

Vaccination and sample collection

All procedures used in animal studies were approved by the Committee on Animal Care at the Massachusetts Institute of Technology and the La Jolla Institute for Allergy and Immunology Animal Care Committee and were consistent with local, state, and federal regulations prior to initiation of this research. Female C57BL/6 mice (8-10 weeks old, Jackson Laboratories) were subcutaneously (s.c) injected at the base of the tail with indicated doses of gp120 and MPLA in 100 µL phosphate-buffered saline (PBS) at the specified doses and days. This injection location drains to the inguinal lymph nodes,

which were collected post-mortem for certain analyses. Alternatively, mice were injected via intramuscular with gp120 formulated in 100ug Alum (Adju-Phos®, Brenntag Biosector A/S).

For SOSIP trimer immunizations, 6-8-week-old 129S1/SvImJ mice (Jackson Laboratories) were used. Mice were given interscapular bolus immunizations with 20 μg BG505 SOSIP.664 gp140 in 0.5 Units of ISCOMATRIX (CSL Ltd.). Osmotic pumps containing 100 μg (2-week slow release) or 50 μg (1-week slow release) BG505 SOSIP.664 gp140 in 0.5 Units of ISCOMATRIX were subcutaneously implanted in the interscapular region. Blood (from retro-orbital or submandibular; 100 μL) was collected weekly into serum separator tubes (BD Corporation) and centrifuged at 4,000 rpm for 10 min at 4˚C. Alternatively, blood was collected in Eppendorf tubes and centrifuged at 13,000 rpm for 30 minutes at 4˚C. Sera extracted from blood samples were stored at -80°C until ready for analysis.

ELISA

Serum anti-gp120 IgG antibodies were quantified by endpoint enzyme-linked immunosorbent assay (ELISA) using gp120 as the capture antigen on 96-well Maxisorp microtiter plates (Nunc). Plates were incubated with 0.5 mg/mL poly-L-lysine in PBS for 4 hrs at room temperature, blocked by 1% BSA in PBS overnight at 4 °C and incubated with 50 nM gp120 in PBS with 1% BSA for 2 hrs at room temperature. Mouse sera was diluted in PBS with 1% BSA at 1:3000 or 1:30000 and incubated for 1.5 hr at 25°C followed by HRP-conjugated goat anti-mouse IgG (1:5000 in PBS with 1% BSA) for 1 hr at 25°C. Plates were washed 4 times in between each step with 0.05% tween-20 in PBS.

Plates were developed with TMB, stopped with 1M sulfuric acid and read at 450 nm and 570 nm using a Tecan M1000 plate reader. Anti-gp120 IgG antibody concentrations were calculated based on ELISA standards using mb12, a monoclonal murine antibody from the NIH AIDS Reagent repository. Analysis was done by subtracting the 570 signal from the 450 nm signal, fitting the standard to a four-parameter log-logistic model with the drc package in R, and using that fit to compute antibody concentrations.

Serum anti-BG505 SOSIP.664 gp140 IgG titers were quantified as previously described (39). Briefly, 96-well MaxiSorp plates (Thermo Scientific) were coated with 5 μg/ml D7324 (Aalto Bio Reagents Ltd) overnight at 4°C. After blocking with 2% skim milk, 0.3 μg/ml C-terminus D7324-tagged BG505 SOSIP.664 trimers were added followed by mouse serum and HRP-labeled goat anti-mouse IgG, Fcγ fragment specific (Jackson ImmunoResearch) with washes in between each step. For V3 specific ELISAs, plates were coated overnight at 4°C with 2 μg/ml BG505 V3 peptide (TRPNNNTRKSIRIGPGQAFYATG) in PBS. After blocking, mouse serum was added followed by HRP-labeled goat anti-mouse IgG with washes in between each step. Colorimetric detection was performed using a TMB substrate kit (Thermo Scientific) and stopped with 2N sulfuric acid. Absorbance was read at 450 nm. Endpoint titers were calculated in GraphPad Prism after subtracting the average background optical density (OD) from all values measured at 450 nm.

Flow cytometry analysis of lymph nodes

Inguinal and brachial lymph nodes were harvested and single cell suspensions were obtained by passage of the lymph nodes though a 70um filter (BD Biosciences). Cells

were washed with PBS and labeled with Live/Dead Aqua (Life Technologies) for 15 min at 25°C. For B-cell activation and germinal center analysis, samples were treated with anti-CD16/32 (TruStain fcX, BioLegend), followed by staining with anti-CD3e-PerCP-Cy5.5 (BD Biosciences), anti-B220-PE-Cy7 (eBioscience), anti-CD138-PE (BD Biosciences), anti-IgD-APC (eBioscience), anti-GL7-FITC (BD Biosciences), anti-MHCII-AF700 (BioLegend), anti-CD86-V450 (BD Biosciences) and PNA-biotin (VectorLabs) + Streptavidin-APCeF780 (eBioscience). CXCR5 stains were performed as previously described (59). Flow cytometry was carried out on a BD LSR Fortessa or LSR II.

Histology of lymph nodes

Inguinal lymph nodes were harvested, embedded in OCT compound, and frozen on dry ice. Frozen tissues were sectioned at 10 um thickness, fixed with 4% PFA, and stained with biotinylated anti-B220 (BioXCell), Streptavidin-APC (BD Biosciences), anti-GL7-FITC (BioLegend) and anti-FITC-AF488 (Jackson ImmunoResearch) for germinal center visualization. Samples were imaged with a PerkinElmer Ultraview Spinning Disk Confocal using a 40x oil objective with a Hammamatsu ORCA-ER CCD camera.

Antigen draining experiments

Gp120 was labeled with IRDye 800CW-NHS (LI-COR Biosciences) following the manufacturer's instructions. Subsequently mice were vaccinated with labeled gp120 in the same manner as before according to the dosing profiles in Fig. 4. Mice were sacrificed and their inguinal lymph nodes were removed. The lymph nodes were digested and fluorescence was measured using a LI-COR Odyssey CLx Infrared Imaging System (LI-

COR Biosciences). Alternatively, mice were vaccinated with intact Phycoerythrin (PE) protein and MPLA as per the aforementioned exp-inc dosing profile or bolus injections, and with 10 μg of BV421 labelled anti-CD21/35 antibody (to label the follicular dendritic cells *in vivo*) 48 hr following the bolus or 48 hr following the last exp-inc injection. Sixteen hours after anti-CD21/35 injections, mice were euthanized and lymph nodes were extracted and processed to visualize the sub-nodal distribution of PE relative to FDC in whole intact lymph nodes using the 3DISCO tissue-clearing method (60). Briefly, lymph nodes were fixed in 4% paraformaldehyde for 2 days, washed and cleared using the DISCO solvents, and subsequently imaged using an Olympus Fluoview FV1200 microscope equipped with 30X (NA 1.05) objective. The images were then processed and reconstructed using Fiji image analysis software. Z-stacks were acquired for individual FDC clusters. Maximum intensity projections were prepared to show the distribution of antigen across the cluster.

Germinal center model calculations

The computational model coarse-grained antigen transport/clearance, the germinal center reaction and antibody production by plasma cells. The model is expressed in terms of a set of chemical reactions between species, including the four key reactions detailed in Figure 3B. Parameters used for the model were collected from the literature and are listed in Table 2, with the exception of the plasma cell antibody secretion rate k. This single parameter was fit to reproduce the 5 IgG measurements made at day 7 and day 14 from each dosing strategy. The confidence interval of the best-fit parameter was $1.89*10^6 - 3.16*10^6$. Measurements before the boost injection at day 21 were chosen to

fit the parameter since the model does not include memory B cells and thus, the effect of their reactivation upon boost. Evolution of these reactions in time was determined by computationally solving a set of partial differential equations describing the temporal evolution of these reactions (Table 2.3) using Matlab; the results were robust with respect to a range of initial conditions.

Table 2.3. The equations underlying the computational model.

Time from initial injection < 6 days	Time from initial injection ≥ 6 days
$\frac{dC_{Ag}}{dt} = F(t) - D_{Ag}C_{Ag} - \beta 1 C_{Ag} C_{IgM}$	$\frac{dC_{Ag}}{dt} = F(t) - D_{Ag}C_{Ag} - (\beta 2 C_{Ag} C_{IgG} + \beta 1 C_{Ag} C_{I\ M})$
$\frac{dC_{IC}}{dt} = \beta 1 C_{\square g} C_{IgM} - D_{IC}C_{IC}$	$\frac{dC_{IC}}{dt} = (\beta 2 C_{Ag} C_{IgG} + \beta 1 C_{Ag} C_{IgM}) - D_{IC}C_{IC} - \beta 2 \gamma C_{IC}$
$\frac{dC_{IgM}}{dt} = -\beta 1 C_{Ag} C_{IgM} - D_{Ab} C_{IgM}$	$\frac{dC_{IgM}}{dt} = -\beta 1 C_{Ag} C_{IgM} - D_{Ab} C_{IgM}$
$\frac{dC_{IgG}}{dt} = 0$	$\frac{dC_{IgG}}{dt} = -\beta 2 C_{Ag} C_{IgG} - D_{Ab} C_{IgM} + k C_{PC}$
	$\frac{dC_{PC}}{dt} = \beta 2 \gamma C_{IC} - D_{PC} C_{PC}$

Statistical Analysis

Error bars are given as standard error of the mean of the log-transformed data. Kruskal-Wallis test with Dunn's *post-hoc* test, or two-way analysis of variance (ANOVA) with Dunnett's *post-hoc* test was used to account for multiple comparisons in computing confidence intervals. *p* values were determined by unpaired Mann-Whitney test. Data was plotted and analyzed with GraphPad Prism and R.

References

1. Barnighausen T, Bloom DE, Cafiero-Fonseca ET, & O'Brien JC (2014) Valuing vaccination. *Proc Natl Acad Sci U S A* 111(34):12313-12319.
2. Nabel GJ (2013) Designing tomorrow's vaccines. *N Engl J Med* 368(6):551-560.
3. Correia BE, *et al.* (2014) Proof of principle for epitope-focused vaccine design. *Nature* 507(7491):201-206.
4. McGuire AT, *et al.* (2013) Engineering HIV envelope protein to activate germline B cell receptors of broadly neutralizing anti-CD4 binding site antibodies. *J Exp Med* 210(4):655-663.
5. Reed SG, Orr MT, & Fox CB (2013) Key roles of adjuvants in modern vaccines. *Nat Med* 19(12):1597-1608.
6. Rerks-Ngarm S, *et al.* (2009) Vaccination with ALVAC and AIDSVAX to prevent HIV-1 infection in Thailand. *N Engl J Med* 361(23):2209-2220.
7. Bojang KA, *et al.* (2001) Efficacy of RTS,S/AS02 malaria vaccine against Plasmodium falciparum infection in semi-immune adult men in The Gambia: a randomised trial. *Lancet* 358(9297):1927-1934.
8. Burton DR & Mascola JR (2015) Antibody responses to envelope glycoproteins in HIV-1 infection. *Nat Immunol* 16(6):571-576.
9. Crotty S (2014) T follicular helper cell differentiation, function, and roles in disease. *Immunity* 41(4):529-542.
10. Ueno H, Banchereau J, & Vinuesa CG (2015) Pathophysiology of T follicular helper cells in humans and mice. *Nat Immunol* 16(2):142-152.

11. Kasturi SP, *et al.* (2011) Programming the magnitude and persistence of antibody responses with innate immunity. *Nature* 470(7335):543-547.
12. Moon JJ, *et al.* (2012) Enhancing humoral responses to a malaria antigen with nanoparticle vaccines that expand Tfh cells and promote germinal center induction. *Proc Natl Acad Sci U S A* 109(4):1080-1085.
13. Baumjohann D, *et al.* (2013) Persistent antigen and germinal center B cells sustain T follicular helper cell responses and phenotype. *Immunity* 38(3):596-605.
14. Victora GD, *et al.* (2010) Germinal center dynamics revealed by multiphoton microscopy with a photoactivatable fluorescent reporter. *Cell* 143(4):592-605.
15. Butler NS, *et al.* (2012) Therapeutic blockade of PD-L1 and LAG-3 rapidly clears established blood-stage Plasmodium infection. *Nat Immunol* 13(2):188-195.
16. Francica JR, *et al.* (2015) Analysis of immunoglobulin transcripts and hypermutation following SHIV(AD8) infection and protein-plus-adjuvant immunization. *Nature communications* 6:6565.
17. Lin WH, Kouyos RD, Adams RJ, Grenfell BT, & Griffin DE (2012) Prolonged persistence of measles virus RNA is characteristic of primary infection dynamics. *Proc Natl Acad Sci U S A* 109(37):14989-14994.
18. Simon ID, Publicover J, & Rose JK (2007) Replication and propagation of attenuated vesicular stomatitis virus vectors in vivo: vector spread correlates with induction of immune responses and persistence of genomic RNA. *J Virol* 81(4):2078-2082.
19. Luker KE, Hutchens M, Schultz T, Pekosz A, & Luker GD (2005) Bioluminescence imaging of vaccinia virus: effects of interferon on viral replication and spread. *Virology* 341(2):284-300.

20. Pape KA, Catron DM, Itano AA, & Jenkins MK (2007) The humoral immune response is initiated in lymph nodes by B cells that acquire soluble antigen directly in the follicles. *Immunity* 26(4):491-502.
21. Gupta RK (1998) Aluminum compounds as vaccine adjuvants. *Adv Drug Deliv Rev* 32(3):155-172.
22. Dupuis M, McDonald DM, & Ott G (1999) Distribution of adjuvant MF59 and antigen gD2 after intramuscular injection in mice. *Vaccine* 18(5-6):434-439.
23. Hutchison S, *et al.* (2012) Antigen depot is not required for alum adjuvanticity. *The FASEB Journal* 26(3):1272-1279.
24. Wang S, *et al.* (2015) Manipulating the selection forces during affinity maturation to generate cross-reactive HIV antibodies. *Cell* 160(4):785-797.
25. Mata-Fink J, *et al.* (2013) Rapid conformational epitope mapping of anti-gp120 antibodies with a designed mutant panel displayed on yeast. *J Mol Biol* 425(2):444-456.
26. Lyumkis D, *et al.* (2013) Cryo-EM structure of a fully glycosylated soluble cleaved HIV-1 envelope trimer. *Science* 342(6165):1484-1490.
27. Julien JP, *et al.* (2013) Crystal structure of a soluble cleaved HIV-1 envelope trimer. *Science* 342(6165):1477-1483.
28. Sanders RW, *et al.* (2013) A next-generation cleaved, soluble HIV-1 Env trimer, BG505 SOSIP.664 gp140, expresses multiple epitopes for broadly neutralizing but not non-neutralizing antibodies. *PLoS pathogens* 9(9):e1003618.
29. Garcon N & Van Mechelen M (2011) Recent clinical experience with vaccines using MPL- and QS-21-containing adjuvant systems. *Expert Rev Vaccines* 10(4):471-486.

30. Kool M, Fierens K, & Lambrecht BN (2012) Alum adjuvant: some of the tricks of the oldest adjuvant. *Journal of medical microbiology* 61(Pt 7):927-934.
31. Carroll MC (1998) The role of complement and complement receptors in induction and regulation of immunity. *Ann. Rev. Immunol.* 16:545-568.
32. Boes M (2000) Role of natural and immune IgM antibodies in immune responses. *Mol Immunol* 37(18):1141-1149.
33. Tew JG & Mandel TE (1979) Prolonged antigen half-life in the lymphoid follicles of specifically immunized mice. *Immunology* 37:69-76.
34. Song H, Nie X, Basu S, & Cerny J (1998) Antibody feedback and somatic mutation in B cells: regulation of mutation by immune complexes with IgG antibody. *Immunol Rev* 162:211-218.
35. Szakal AK, Kosco MH, & Tew JG (1988) FDC-iccosome mediated antigen delivery to germinal center B cells, antigen processing and presentation to T cells. *Adv Exp Med Biol* 237:197-202.
36. Dixit NM, Srivastava P, & Vishnoi NK (2012) A Finite Population Model of Molecular Evolution: Theory and Computation. *Journal of Computational Biology* 19:1176-1202.
37. Corti D, *et al.* (2011) A neutralizing antibody selected from plasma cells that binds to group 1 and group 2 influenza A hemagglutinins. *Science (New York, N.Y.)* 333:850-856.
38. Sanders RW, *et al.* (2015) HIV-1 VACCINES. HIV-1 neutralizing antibodies induced by native-like envelope trimers. *Science* 349(6244):aac4223.
39. Hu JK, *et al.* (2015) Murine antibody responses to cleaved soluble HIV-1 envelope trimers are highly restricted in specificity. *J Virol.*

40. Amanna IJ & Slifka MK (2011) Contributions of humoral and cellular immunity to vaccine-induced protection in humans. *Virology*:1-10.
41. Cubas RA, *et al.* (2013) Inadequate T follicular cell help impairs B cell immunity during HIV infection. *Nat Med* 19(4):494-499.
42. Yamamoto T, *et al.* (2015) Quality and quantity of TFH cells are critical for broad antibody development in SHIVAD8 infection. *Sci Transl Med* 7(298):298ra120.
43. Locci M, *et al.* (2013) Human circulating PD-1+CXCR3-CXCR5+ memory Tfh cells are highly functional and correlate with broadly neutralizing HIV antibody responses. *Immunity* 39(4):758-769.
44. Dosenovic P, *et al.* (2015) Immunization for HIV-1 Broadly Neutralizing Antibodies in Human Ig Knockin Mice. *Cell* 161(7):1505-1515.
45. Haynes BF, Kelsoe G, Harrison SC, & Kepler TB (2012) B-cell-lineage immunogen design in vaccine development with HIV-1 as a case study. *Nat Biotechnol* 30(5):423-433.
46. Moyer TJ, Zmolek AC, & Irvine DJ (2016) Beyond antigens and adjuvants: formulating future vaccines. *J Clin Invest* 126(3):799-808.
47. Kemp JM, *et al.* (2002) Continuous antigen delivery from controlled release implants induces significant and anamnestic immune responses. *Vaccine* 20(7-8):1089-1098.
48. Spiers ID, Eyles JE, Baillie LW, Williamson ED, & Alpar HO (2000) Biodegradable microparticles with different release profiles: effect on the immune response after a single administration via intranasal and intramuscular routes. *The Journal of pharmacy and pharmacology* 52(10):1195-1201.

49. Thomasin C, Corradin G, Men Y, Merkle H, & Gander B (1996) Tetanus toxoid and synthetic malaria antigen containing poly (lactide)/poly (lactide-co-glycolide) microspheres: importance of polymer degradation and antigen release for immune response. *Journal of Controlled Release* 41(1-2):131-145.

50. Preis I & Langer RS (1979) A single-step immunization by sustained antigen release. *J Immunol Methods* 28(1-2):193-197.

51. Johansen P, *et al.* (2008) Antigen kinetics determines immune reactivity. *Proceedings of the National Academy of Sciences of the United States of America* 105(13):5189-5194.

52. Demuth PC, Garcia-Beltran WF, Ai-Ling ML, Hammond PT, & Irvine DJ (2013) Composite dissolving microneedles for coordinated control of antigen and adjuvant delivery kinetics in transcutaneous vaccination. *Advanced functional materials* 23(2):161-172.

53. Pekarek KJ, Jacob JS, & Mathiowitz E (1994) Double-walled polymer microspheres for controlled drug release. *Nature* 367:258-260.

54. Prescott JH, *et al.* (2006) Chronic, programmed polypeptide delivery from an implanted, multireservoir microchip device. *Nature biotechnology* 24:437-438.

55. Xia Y & Pack DW (2014) Pulsatile protein release from monodisperse liquid-core microcapsules of controllable shell thickness. *Pharmaceutical research* 31:3201-3210.

56. Ford Versypt AN, Pack DW, & Braatz RD (2013) Mathematical modeling of drug delivery from autocatalytically degradable PLGA microspheres--a review. *Journal of controlled release : official journal of the Controlled Release Society* 165:29-37.

57. Soppimath KS, Aminabhavi TM, Kulkarni AR, & Rudzinski WE (2001) Biodegradable polymeric nanoparticles as drug delivery devices. *Journal of Controlled Release* 70:1-20.

58. Chung NP, *et al.* (2014) Stable 293 T and CHO cell lines expressing cleaved, stable HIV-1 envelope glycoprotein trimers for structural and vaccine studies. *Retrovirology* 11:33.

59. Choi YS, *et al.* (2011) ICOS receptor instructs T follicular helper cell versus effector cell differentiation via induction of the transcriptional repressor Bcl6. *Immunity* 34(6):932-946.

60. Erturk A, *et al.* (2012) Three-dimensional imaging of solvent-cleared organs using 3DISCO. *Nat Protoc* 7(11):1983-1995.

61. Mandel TE, *et al.* (1980) The follicular dendritic cell: long term antigen retention during immunity. *Immunol Rev* 53:29-59.

62. Mankarious S, *et al.* (1988) The half-lives of IgG subclasses and specific antibodies in patients with primary immunodeficiency who are receiving intravenously administered immunoglobulin. *J Lab Clin Med* 113(5):634-640.

63. Kepler TB & Perelson AS. (1993) Cyclic re-entry of germinal center B cells and the efficiency of affinity maturation. *Immunol Today* 14(8):412-415.

64. Meyer-Hermann M, *et al.* (2012) A Theory of Germinal Center B Cell Selection, Division, and Exit. *Cell Rep* 2(1)162-174.

65. Meyer-Hermann M, Maini PK, Iber D. (2006) An analysis of B cell selection mechanisms in germinal centers. *Math Med Biol* 23(3):255-277.

66. Zhang J & Shakhnovich EI. (2010) Optimality of mutation and selection in germinal centers. *PLoS Comput Biol* 6(6): e1000800.

67. Proulx ST, *et al.* (2007) MRI and Quantification of Draining Lymph Node Function in Inflammatory Arthritis. *Ann. N. Y. Acad. Sci* 1117: 106–123.

68. Townsley-Fuchs J, *et al.* (1996) Human Immunodeficiency Virus-1 (HIV-1) gp120 Superantigen-binding Serum Antibodies. *J Clin Invest.* 98(8):1794-1801.

Chapter 3: Chlorotoxin-siRNA conjugate delivery to brain tumors

Overview

Glioblastoma is an aggressive type of brain tumor with a high mortality rate. It has an incidence rate of 5.26 per 100,000, and is the most common primary malignant brain tumor(2). Despite recent advances in treatment, it remains a disease with high mortality. In a recent analyses of cases in the Netherlands and the US, the two-year survival remains at approximately14% and five-year survival is less than 5%(3, 4). This is due to several factors, including its resistance to current treatments and the inherent difficulty of neurosurgery(2). Approaches that tackle the disease at the molecular level through altered expression of oncogenes and other proteins contributing to drug/radiation resistance can potentially provide new opportunities for treatments that result in better outcomes for patients(5).

Small interfering RNAs (siRNAs) are a class of nucleic acid drugs that can be used to decrease expression of specific genes using the RNA interference pathway(6). In brief, when short, double-stranded RNA is in the cytoplasm, it is cleaved by a protein complex called DICER. One strand is then loaded onto the RNA-induced silencing complex (RISC), which finds and cleaves mRNAs complementary to the loaded strand. This leads to sequence-specific knockdown of the targeted gene. Due to the versatility of this pathway, siRNA can be used to treat a wide variety of diseases caused by overexpression of a gene.

However, siRNA itself is a highly-charged molecule that does not cross biological membranes and is excreted from the kidneys(7). The major barrier to using siRNA as a treatment in the clinic is primarily delivery into the correct cell type. Many delivery technologies have been evaluated for delivering siRNA to tissues of interest. These

include viral vectors, lipid and polymer nanoparticles, polyplexes, and conjugates to small molecules, proteins, and aptamers(7–9). While these technologies have been successful in delivering siRNA to the liver, endothelium, and subcutaneous tumors, there has been limited success in delivery siRNA through the blood-brain barrier. There has been even less reported success in delivering siRNA to orthotopic brain tumors in animal models(8). Since the nucleic acid sequence generally does not affect the transport properties of siRNA, technologies that enable delivery could be used to knock down a wide range of genes. Thus, siRNA could be deployed against single or multiple gene targets in a wide range of processes in cancer, including genes involved in remodeling, metastasis, and growth(5).

Development of siRNA conjugates

We chose to develop siRNA conjugate systems because some of the leading siRNA clinical candidates are conjugates of siRNA with a triple galactose-N-acetaldehyde (GalNAc) ligand that is effective in delivering siRNA to the liver(10). Furthermore, conjugates have a defined chemical structure allowing for easier manufacturing and quality control. Also, smaller siRNA conjugates are more likely to cross the blood-brain/blood tumor barrier. Lastly, conjugates can also be administered subcutaneously, which is more pleasant for the patient compared to intravenous administration, which is required for many nanoparticle siRNA formulations.

To develop a conjugate delivery system for siRNA to brain tumors, we turned to molecular imaging agents that have been shown to target brain tumors. Chlorotoxin is a 4 kDa peptide derived from the venom of the *Leiurus quinquestriatus* scorpion(11, 12). It has been shown to traffic through the blood-brain barrier and bind to a variety of tumors due

to its affinity for MMP-2 and Annexin A2(11, 13). Indeed, one study found chlorotoxin binding in 34 categories of tumors, which include brain, skin, prostate, breast, and colorectal cancers, among others(11). Currently, BLZ-100, which is Cy5.5-labeled chlorotoxin, is in clinical trials for fluorescently "painting" skin, central nervous system, and other solid tumors so that surgeons can visualize the tumor margin(14). Other imaging agents are being developed as well(15).

Chemistry of siRNA conjugates

The generic reaction scheme for the synthesis of chlorotoxin (CTX)-siRNA conjugates is outlined in Figure 3.1. Briefly, we attach a PEG-azide to CTX through an amine, and then react the CTX-PEG-azide with DBCO-modified siRNA to form the conjugate. We chose to use strain-promoted azide-alkyne cycloaddition for the conjugation due to its high yield, bioorthogonality, and to protect the siRNA and CTX from denaturing in other solvents(16). PEG linkers were chosen for their biocompatibility and flexibility. Following synthesis, CTX-PEG-azide and CTX-PEG-siRNA conjugates were assayed for purity using RP-HPLC and for molecular weight using MALDI-TOF, confirming the desired CTX-siRNA conjugates (Figure 3.2).

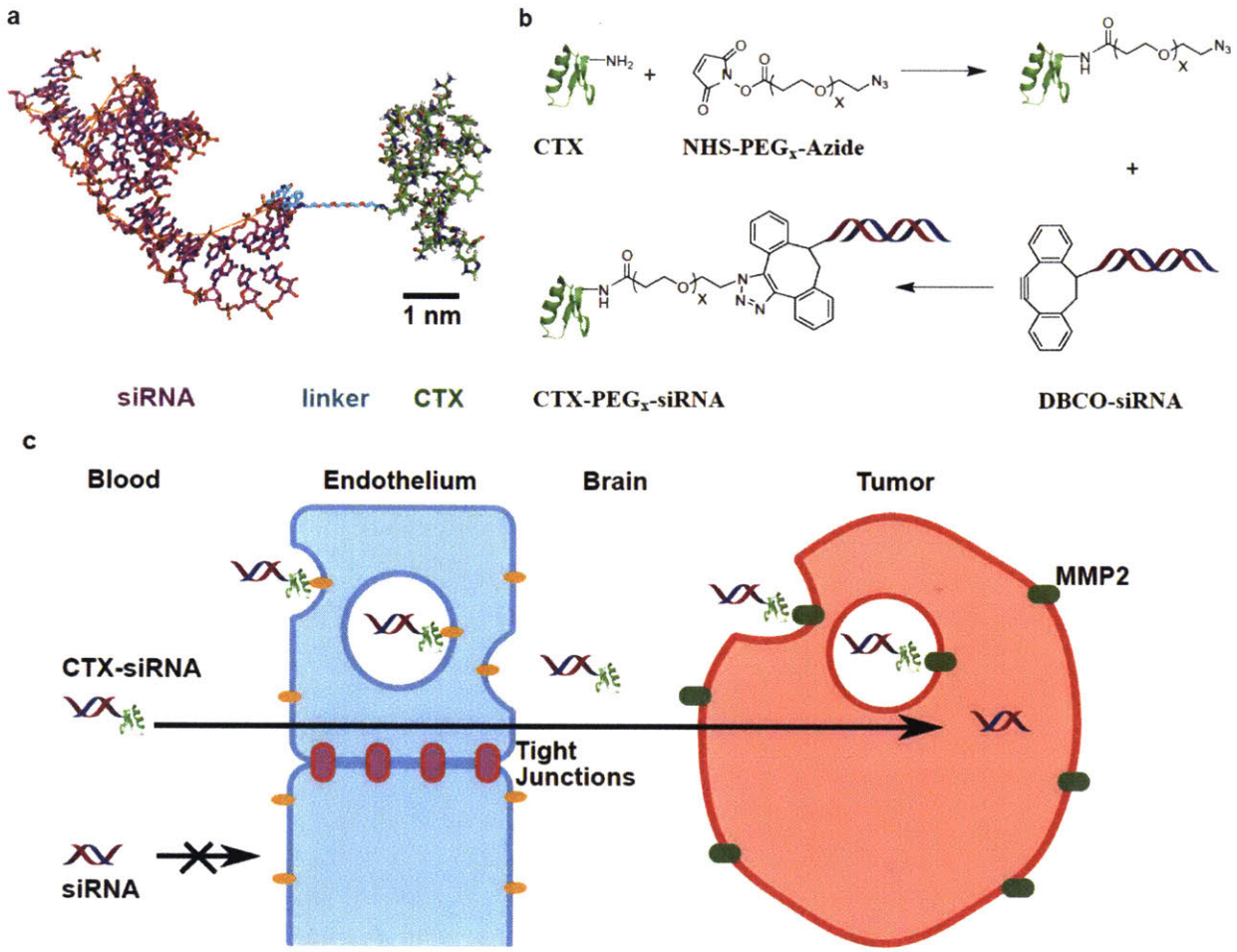

Figure 3.1. Synthesis of chlorotoxin-siRNA conjugates.
a) Schematic of the chlorotoxin-PEG-siRNA conjugate with scale bar. b) Reaction scheme to synthesize chlorotoxin-siRNA conjugates. Briefly, CTX was reacted with NHS-PEG-Azide to yield CTX-PEG-Azide. This was purified by RP-HPLC to yield singly labeled CTX. CTX-PEG-Azide was then reacted with DBCO-siRNA to yield CTX-PEG-siRNA, which was further purified by RP-HPLC. CTX, chlorotoxin. c) Schematic of how the drug delivery system works. siRNA cannot pass through the blood-brain barrier due to its size and charge. However, CTX-PEG-siRNA is transcytosed through the brain endothelium, likely through interaction with ANXA2 or some other protein, and then it binds to MMP2 on tumors. It is then endocytosed, survives the endosome due to the stability of the siRNA, and is released into the cytoplasm, where it can knock down the gene of interest.

In vitro testing of siRNA conjugates

To determine whether or not the conjugates entered cells, we synthesized conjugates with Cy5.5-labeled siRNAs and dosed U87-MG cells (a common human glioblastoma cell

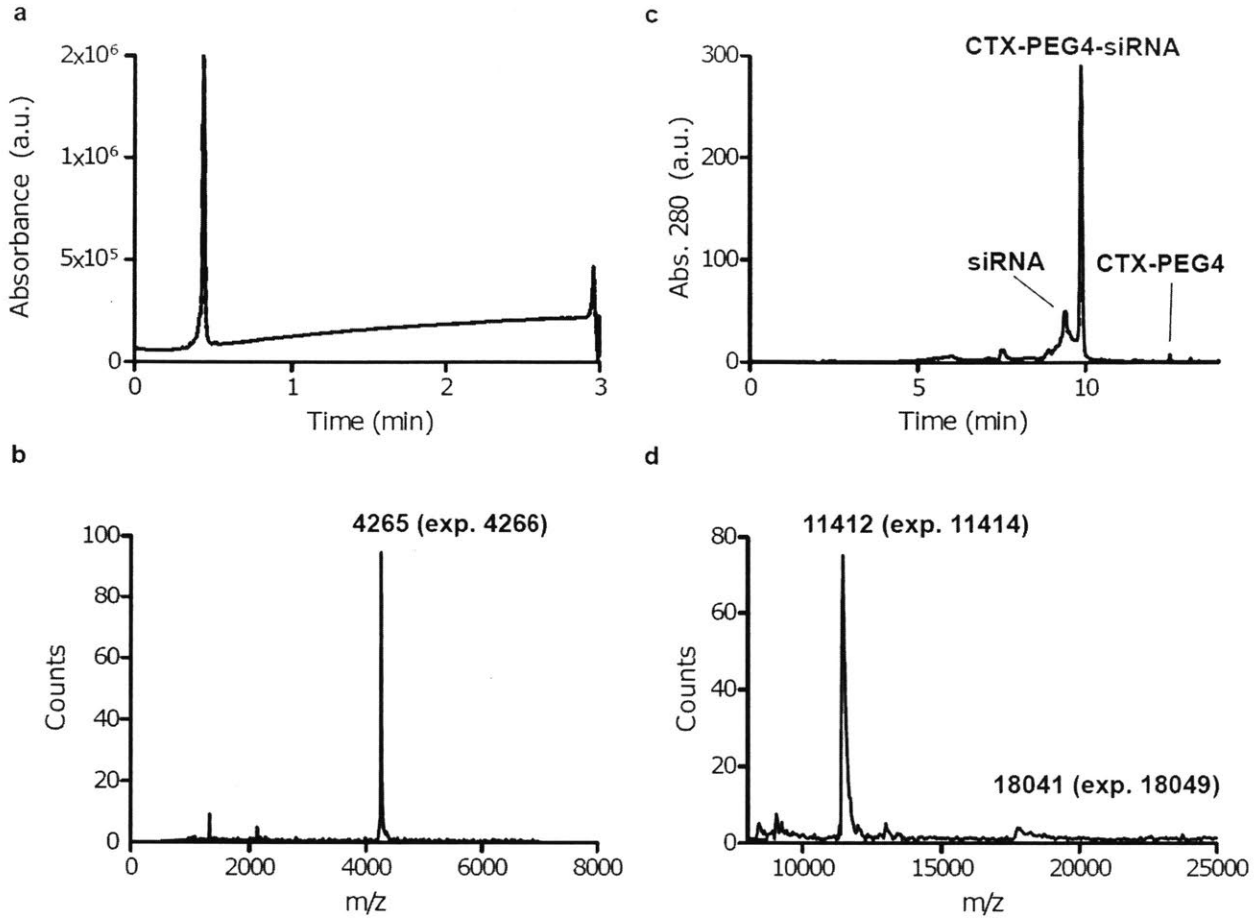

Figure 3.2. Characterization of chlorotoxin conjugates.
a) RP-HPLC analysis of CTX-PEG4-azide on a Waters LC/MS. b) MALDI-TOF trace of CTX-PEG4-azide. C) RP-HPLC analysis of CTX-PEG4-AHA1. d) MALDI-TOF trace of CTX-PEG4-azide. First peak from left is single-stranded CTX-PEG4-AHA1-antisense strand. Second peak labeled is double-stranded CTX-PEG4-AHA1. Note that double-stranded RNA is much less stable under MALDI conditions and thus the peak at 18049 is much smaller. Matrix used was HPA.

line(17)) transfected with Luc and GFP for 1 hr with 1 μM of fluorescent conjugate or unconjugated fluorescent siRNA. The cells were then imaged to determine whether the conjugates were endocytosed by the cells (Figure 3.3A). From the obtained images, we can observe that more of the CTX-PEG4-siRNA conjugates were endocytosed relative to the unconjugated siRNA.

We then synthesized a series of CTX-PEG-siRNA conjugates with PEG linkers of 4, 12, and 24 units long to optimize the linker length. The siRNA we used targeted the human activator of 90 kDa heat shock protein ATPase homolog 1 (AHA1) gene(18, 19). We chose this siRNA because AHA1 is widely expressed in most cell types. Furthermore, this siRNA was chemically stabilized against degradation by nucleases in vivo, which is an important consideration for conjugates(20). To test knockdown, we treated U87MG-Luc-GFP cells for 72 hours with the conjugates (Figure 3.3B). Our results suggest that there is dose-dependent knockdown of the AHA1 mRNA in the chlorotoxin conjugates, with the most knockdown observed in the CTX-PEG4-AHA1 conjugate (at 5 μM, 46% for PEG4, 7% for PEG12, 24% for PEG24). We did not observe significant knockdown for unconjugated AHA1 siRNA (0% at 2.5 uM).

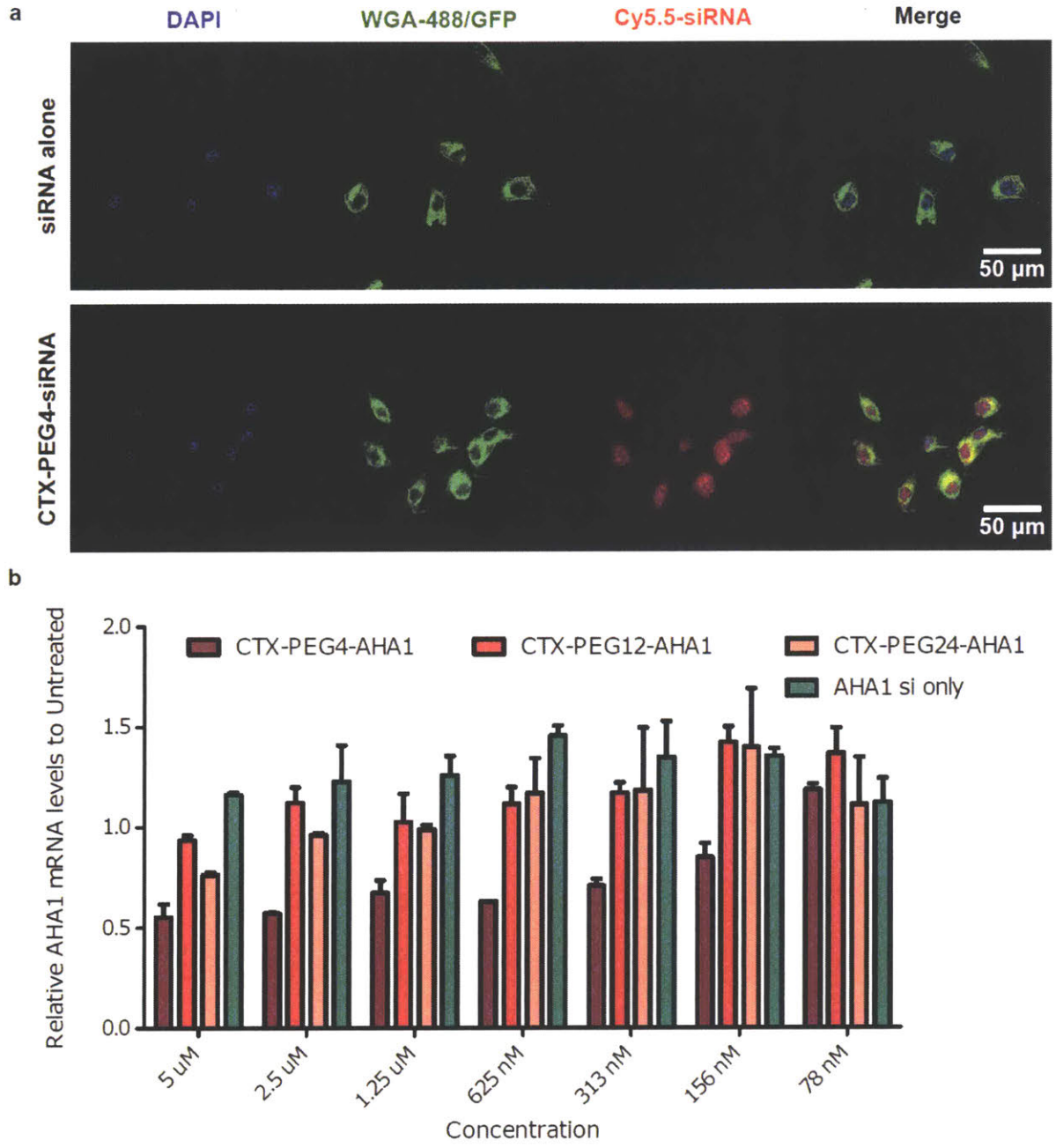

Figure 3.3. In vitro performance of CTX-PEG-siRNA conjugates.
a) Confocal images of U87MG-Luc-GFP cells treated with CTX-PEG-AHA1-Cy5.5 conjugates (bottom) or AHA1-Cy5.5 (top) for 1 hour at 1 µM. Red is the siRNA, green is the cell (GFP expressed in the cell and WGA-488 staining cell membrane glycoproteins), and blue is the nucleus (NucBlue dye). b) Relative AHA1 mRNA in U87MG-Luc-GFP cells treated with CTX-PEG-AHA1 conjugates for 72 hours as measured by the Quantigene mRNA assay. Untreated U87MG-Luc-GFP cells have an mRNA level of 1. mRNA levels were normalized for cell number by ACTB mRNA levels.

In vivo testing of conjugate biodistribution to intracranial tumors

We next evaluated the lead CTX-PEG4-siRNA conjugate vivo using a U87MG-Luc-GFP cell line which allows for cellular visualization through imaging of luciferase and GFP expression. To model tumors in the brain, we implanted the cells intracranially in nude mice and allowed them to develop into tumors. To determine whether the siRNA trafficked to the tumor, we injected the mice either subcutaneously (s.c) or intravenously (i.v.) with Cy5.5-labeled siRNA or conjugates and then removed the tumor and part of the brain after 24 hours. The tissue was dissociated and analyzed by flow cytometry to determine whether the siRNA was present in the tumor cells. Figure 3.4B shows that CTX-siRNA conjugates have greatly improved trafficking to the tumor compared to unconjugated siRNA (mean fluorescence 3216 vs 925, $p = 0.002$) while sparing most mouse cells (3216 vs. 235, $p < 0.001$). Furthermore, we observed that s.c. administration is not significantly different in efficacy to i.v. administration (mean fluorescence 3216 vs. 3789, $p=0.28$). We proceeded with s.c. administration as it is easier for patients to self-administer than i.v. injections.

We then investigated the pharmacokinetics of the siRNA in the tumor after s.c. administration. Mice with or without tumors were treated with either CTX-PEG4-siRNA-

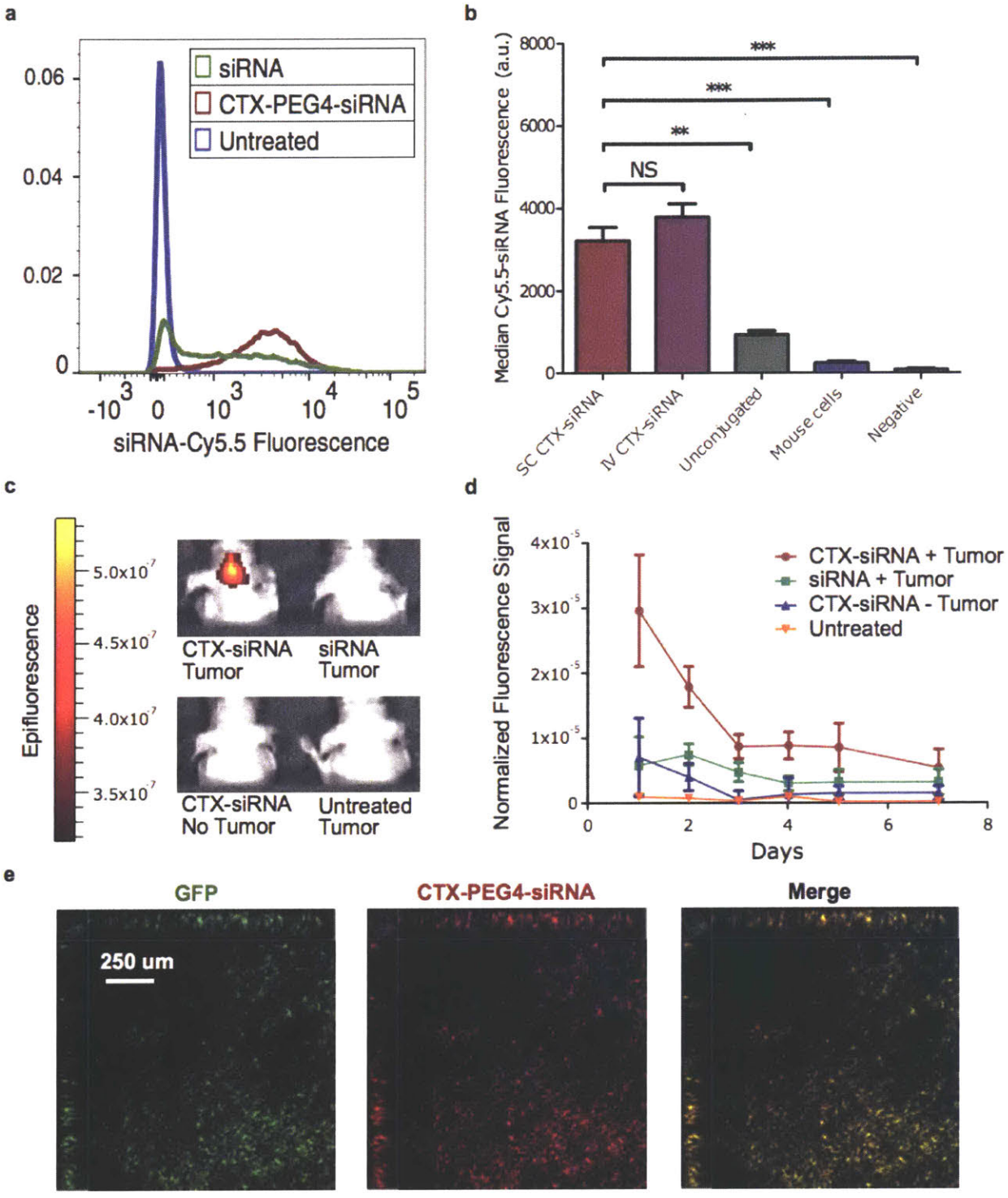

Figure 3.4. In vivo targeting of CTX-PEG-siRNA conjugates to tumor cells in a mouse model of glioblastoma.
Six-week-old nu/nu mice were injected intracranially with U87MG-Luc-GFP cells and treated after the tumor reached 1.5-2 mm in size via luminescence. a) Sample histograms from flow cytometry showing the intensity of CTX-PEG-siRNA-Cy5.5 signal vs. siRNA-Cy5.5 signal in U87MG-GFP-Luc tumors 24 hours after s.c injection. b) Cy5.5 signal intensity in U87MG-GFP-Luc tumors after s.c. injection of CTX-PEG-siRNA-Cy5.5, i.v. injection of CTX-PEG-siRNA-Cy5.5, and i.v. injection of siRNA-Cy5.5. The two rightmost columns are untreated tumor and mouse cell (GFP negative) levels from all injections of CTX-PEG-siRNA-Cy5.5. All samples taken 24 hours post-injection. *P*-values from two-tailed t-tests from left to right are 0.28, 0.002, <0.001, and <0.001. N=3. c) Sample images from IVIS 5 days post s.c. injection of 8 mg/kg of CTX-PEG4-siRNA-Cy5.5. Scale is in radiance efficiency. d) Quantitation of max fluorescence over 7 days post s.c. injection in the area of the tumor (as indicated by luciferase signal) or head area for mice without tumors. NS, not significant. e) Representative images from intravital imaging of tumor field. Green denotes the tumor cells, red denotes the CTX-PEG4-siRNA-Cy5.5 conjugates. Images were acquired 30 mins post i.v. injection of 150 μL of 1 μM CTX-PEG4-siRNA-Cy5.5 solution.

Cy5.5 or siRNA-Cy5.5 and imaged using an IVIS instrument. Cy5.5 fluorescence was measured in the region of the head where the tumor had been implanted for 8 days post-injection. As shown in Figure 3.4D, the fluorescence signal is much stronger in mice with tumors (Day 1 epifluorescence, tumors + CTX-si: 29.5×10^{-6}, tumors + si 5.7×10^{-6}, no tumor + CTX-si: 7.0×10^{-6}, control mice 0.9×10^{-6}), and the siRNA persists for at least one week in the tumor (Day 8 epifluorescence, tumors + CTX-si: 5.3×10^{-6}, tumors + si 3.1×10^{-6}, no tumor + CTX-si: 1.4×10^{-6}). Figure 3.4C shows images from some of the mice on day 5, and although the fluorescence is much lower than day 1, the siRNA is still primarily in the mice with tumors that were treated with CTX-PEG4-siRNA conjugates.

Furthermore, we used intravital imaging to understand how the siRNA is distributed throughout the tumor and whether it can penetrate the tumor. Briefly, mice were anesthetized, a craniotomy was performed, and a slide was placed over the tumor. A multiphoton microscope was used to image the tumor tissue. Figure 3.4E contains

representative wide-field images which show that the conjugate is indeed found within a wide section of the tumor.

Knockdown of housekeeping genes *in vivo* using conjugates

Lastly, we measured RNA knockdown (KD) of our target gene (AHA1) in brain tumor xenografts. This was done 72 hours post-injection, to allow time for trafficking and knockdown. Figure 3.5 shows 7% reduction in AHA1 mRNA in the groups treated with unconjugated siRNA, which was not statistically significantly different from untreated (p=0.55). However, there was a dose-dependent and statistically significant reduction (8 mg/kg: 31% KD, p=0.024; 16 mg/kg: 49% KD, p=0.001) in AHA1 mRNA in the groups treated with CTX-PEG4-siRNA conjugates. This demonstrates that we can successfully knock down genes in a mouse xenograft model of brain tumors.

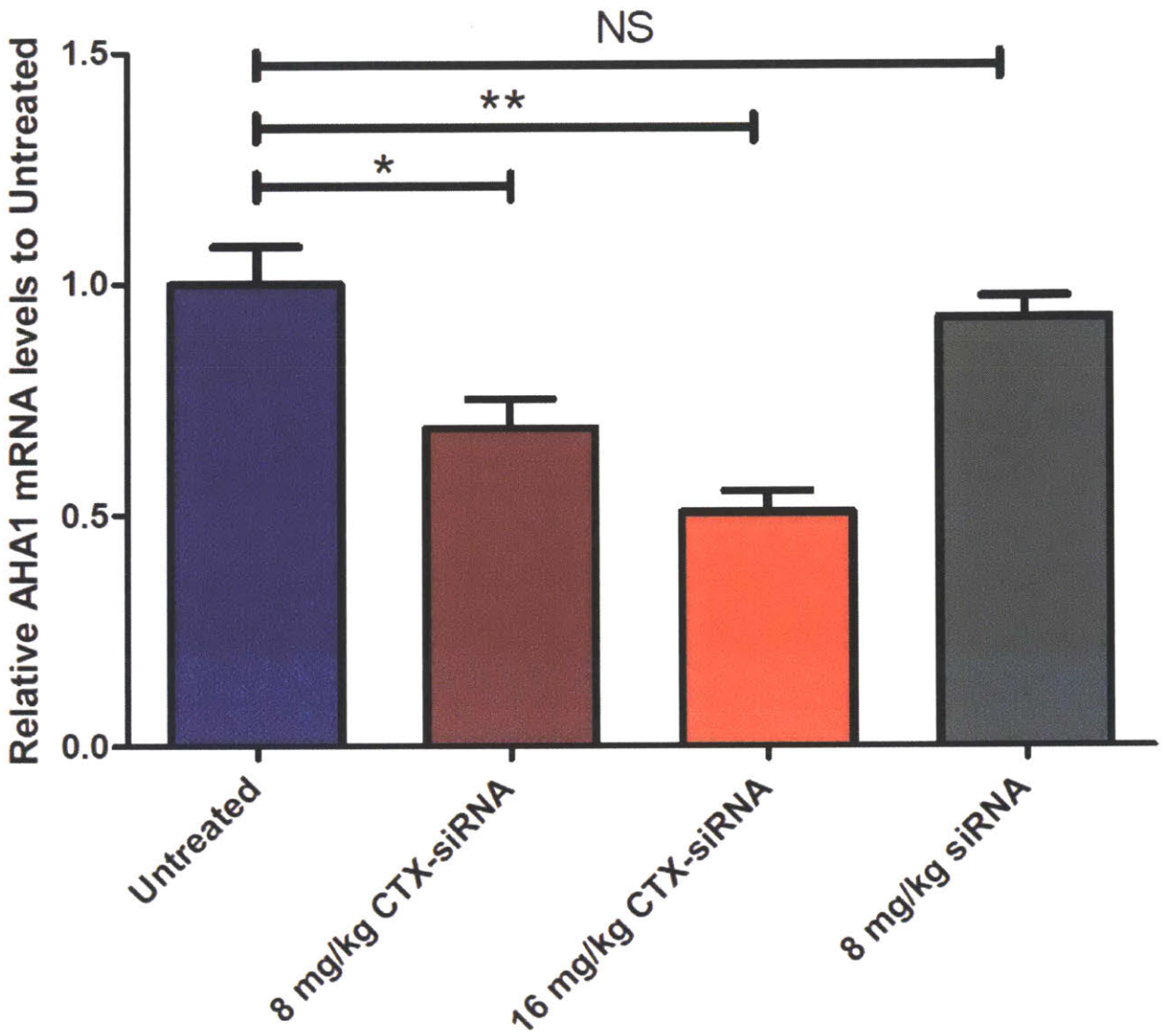

Figure 3.5. In vivo knockdown efficiency in tumor of CTX-PEG4-siRNA conjugates. Six-week-old nu/nu mice were injected intracranially with U87MG-Luc-GFP cells and treated after the tumor reached 1.5-2 mm in size via luminescence. Mice were injected s.c. with CTX-PEG4-AHA1 or unconjugated AHA1 at the specified doses (N=5 for treatment groups, N=9 for untreated). For comparison purposes, doses only consider the mass of the siRNA, not the conjugate. Mice were sacrificed 72 hours post injection, and tumor was resected. mRNA from the tumor was quantified by the Quantigene 2.0 assay using a human-specific probe to probe knockdown in the U87MG-Luc-GFP cells. Untreated tumors have an mRNA level of 1. mRNA levels were normalized for cell number by ACTB mRNA levels. The untreated group was significantly different from the 8 mg/kg CTX-PEG4-AHA1 group (31% KD, p=0.024, t-test, two-tailed) and the 16 mg/kg CTX-PEG4-AHA1 group (49% KD, p=0.001), but not the 8 mg/kg siRNA alone group (7% KD, p=0.548). NS, not significant; KD, knockdown.

Application to CYCLOPS genes

We also attempted to apply the conjugates to a disease-modifying siRNA. Work by Rameen Beroukhim's lab at the Dana Farber Cancer Institute and Broad Institute has shown that RNAi suppression of critical genes that have lost alleles in tumors could be used to kill tumors. These genes, called CYCLOPS genes, are genes that are critical for cell survival and have only one allele present in the cell due to aneuploidy or mutations. Because of this, lower levels of suppression of protein production may be able to decrease survival of the tumor. The system had been proved *in vivo* using genetically modified tumor lines that included Dox-inducible shRNA(21). After administering doxycycline to the mice, there was dose-dependent knockdown of a putative CYCLOPS gene and subsequent reduction in tumor size in the vulnerable cell line. From their publication, for one of the genes, it appeared that the knocking down 50% of the mRNA is enough to get 75-90% loss of cell viability. Since this appeared to be a limit on the amount of knockdown we could obtain with the chlorotoxin-siRNA system, we decided to see if CYCLOPS genes could have a therapeutic effect.

Table 3.1. CYCLOPS genes identified for U87MG cell line

Gene	Function	Prevalence
PABPN1	Part of a complex that adds poly-A tails to mRNA	21% of cancers 30% of GBM
DNAJA3	Mitochondrial chaperone involved in protein folding and degradation	16% of cancers 11% of GBM
SNRPB/C	Required parts of the spliceosome	10/13% of cancers 3/13% of GBM

In collaboration with a postdoc (Brenton Paolella) in his lab, we have identified CYCLOPS genes in the U87 cell line. Table 3.1 lists some of the genes that Brent identified for U87 cells that fulfilled criteria for being CYCLOPS genes.

We purchased siRNAs against these genes from Axolabs GmBH. After screening a variety of siRNAs against these 4 targets *in vitro*, I identified the most potent ones and treated cells with them. Because CYCLOPS genes are ones that have lost alleles, the control we used was the diploid cell line Cal51, a breast cancer line. To determine which CYCLOPS gene had maximal cytotoxicity, I treated U87 and Cal51 cells with a range of doses of the siRNA with Lipofectamine, and then measured cell viability after 72 hours. The results are shown in Figure 3.6.

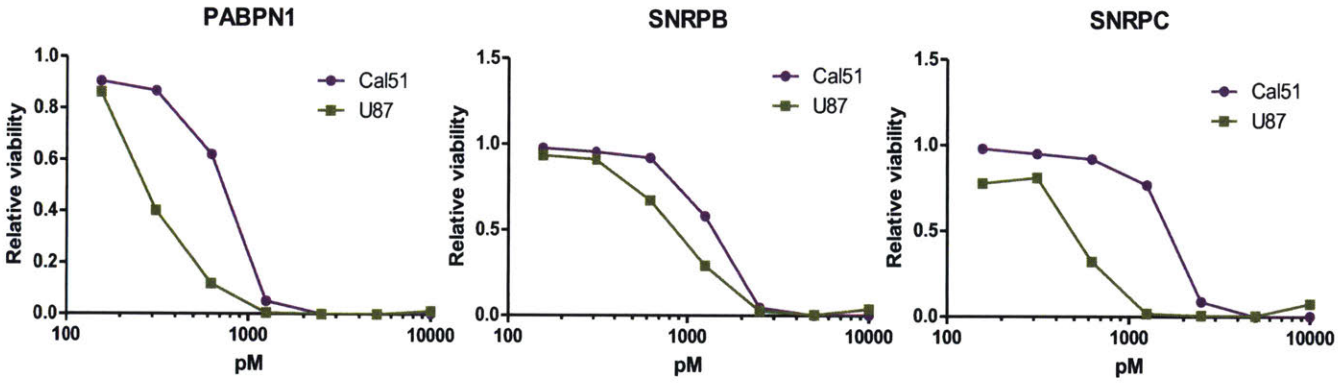

Figure 3.6. In vitro performance of CYCLOPS genes on U87 cells.
Cal51 and U87 cells were plated in 96 well plates at 20,000 per well. Cells were treated with dilutions of siRNA- Lipofectamine RNAiMax lipoplexes created following manufacturer's instructions at the specified siRNA concentration (N=2). Viability was measured 72 hours later using the Cell-Titer Glo assay.

Afterwards, PABPN1 was identified as the optimal conjugate and tested in U87 tumor-bearing nu/nu mice *in vivo*. Unfortunately, as seen in Figure 3.7, it did not have a significant effect on tumor growth. This is likely due to the extremely fast growth rate of the U87 model and glioblastomas in general. Because we are likely to only get an ~50%

reduction in viability in those cells that exhibit knockdown during the procedure, even though we transfect twice, the cells that were not transfected grow faster and outcompete those that do.

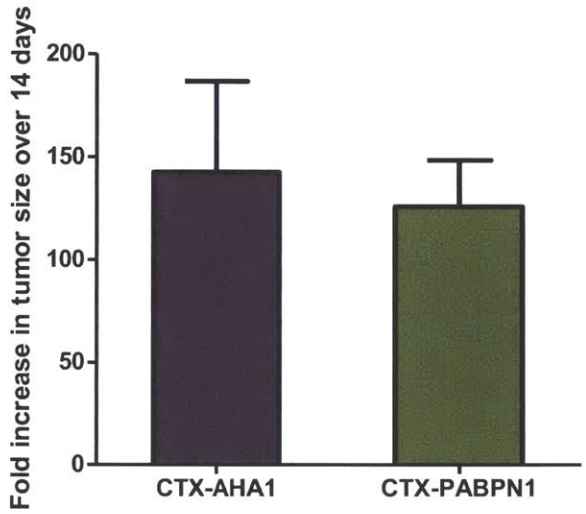

Figure 3.7. In vivo testing of CTX-AHA1 vs CTX-PABPN1.
Mice bearing U87 intracranial tumors were treated subcutaneously with CTX-AHA1 or CTX-PABPN1 at 16 mg/kg on day 4 and day 11 post tumor inoculation. Tumors were imaged using BLI and the IVIS system over 14 days. Y axis is ratio of tumor size at first treatment to tumor size at day 19.

In summary, we present the development of a brain-tumor targeted siRNA conjugate that can knock down genes in vivo. This is a platform that can be used to deliver siRNA against a wide variety of genes into tumor cells in vivo after subcutaneous injection. As chlorotoxin has affinity for many other types of tumors, including breast, ovarian, prostate, and others, this delivery system could be adapted for other tumor types as well(11). We believe this to be the first instance of systemic subcutaneous siRNA delivery and knockdown in an orthotopic mouse xenograft brain tumor model. The ability to specifically deliver siRNA to cancer cells in the brain without the need for a carrier is a powerful new tool for the development of next generation therapies for brain tumors.

Materials and Methods

Synthesis of siRNA-chlorotoxin conjugates

10 mg Chlorotoxin (Alomone Labs, Jerusalem, Israel) was solubilized in ph 8 phosphate buffer at 5 mg/mL. 1.7 mg NHS-PEG-Azide (Quanta BioDesign, Plain City, OH) was dissolved in 222 µL of DMSO and added to the chlorotoxin solution with mixing. The solution was reacted at 4 C overnight and purified by RP HPLC using 1.5% Acetic acid/Acetonitrile phases with a Waters C18 Xbridge Peptide BEH 300A, 3.5 µm column followed by lyophilization to yield fractionated chlorotoxin-PEG-azide. Fractionated chlorotoxin-PEG-azide was solubilized in RNAse-free water and analyzed by LC/MS (Waters) to determine purity and molecular weight.

Dibenzylcyclooctyne (DBCO) modified siRNA (Axo Labs, Kolmbach, Germany) was then added to the purified chlorotoxin-PEG-azide fractions at a 1:1 stoichiometric ratio and reacted overnight at RT to yield chlorotoxin-PEG-siRNA conjugates. Conjugates were purified by RP-HPLC on the same column using 0.1 mM triethylamine-acetic-acid/Acetonitrile phases and analyzed by MALDI-TOF and RP HPLC to determine purity and molecular weight.

Generation of U87MG-Luc-GFP cell line

HEK-293T cells were transfected with pMLS-GFP- Luciferase, VSVG and Gag/Pol packaging vectors using the viral supernatant. The pMLS-EGFP- Firefly Luciferase plasmid was a gift from Michael Yaffe. The viral supernatant was used to transduce U87MG (ATCC) cells for stable expression of EGFP and firefly luciferase. Cells were used for intracranial orthotopic injections after at least 3 passages to dilute out any remaining unintegrated virus particles

In vitro knockdown assays

U87MG-Luc-GFP cells were seeded in a 96-well plate at 25,000 cells per well. Chlorotoxin-PEG-siRNA was added to the cells and left for 72 hours. After 72 hours, the AHA1 and ACTB mRNA content of the cells was analyzed using the Quantigene mRNA assay (Affymetrix) according to the manufacturer's instructions. In the analysis, AHA1 mRNA levels were normalized by ACTB mRNA levels to account for variations in cell loading.

In vitro imaging

U87 cells were plated in an 8-well LabTek II Chamberslide (Nunc) at 25,000 cells per well. After 24 hours, cells were treated with chlorotoxin-PEG-siRNA-Cy5.5 conjugates at 500 nM. After 1 h, cells were washed twice gently with 37 C PBS, fixed in 4% paraformaldehyde solution (Electron Microscopy Sciences) for 10 mins at RT, washed thrice with RT PBS, stained with WGA-488 (Invitrogen) and NucBlue Fixed Cell Stain (Invitrogen) for 20 mins, and washed thrice with RT PBS. The chambers were then removed, and a coverslip was mounted on the slide with Prolong Diamond Antifade (Invitrogen). The slide was left to dry for 48 hours and then imaged on an Olympus FV1200 confocal microscope.

In vivo tumor implantations and experiments

U87-Luc-GFP cells were implanted in 6-8-week-old female nude mice (Charles River) via intracranial injections. An incision was made across the top of the skull, and a small hole was carefully drilled through the skull 2 mm to the right and 2mm caudal to the bregma using an 18G needle. This location was chosen as it is a typical location for tumors to form in patients(22). 150,000 U87MG-GFP-Luc cells in 3 μL PBS were injected over the

course of 3 minutes 3 mm deep into the brain using a Hamilton Neuros Model 75 blunt end 5 μL syringe. The needle was allowed to rest for one minute, and then slowly retracted over 30 seconds. The hole was immediately filled with bone wax, and the incision was closed with Vetbond tissue adhesive (3M). Tumors were measured as they grew via luminescence: mice were injected intraperitoneally (i.p.) with 150 μL of 15 mg/mL D-luciferin solution (Perkin Elmer) and were imaged in an IVIS machine 10 minutes post injection for 1 s at medium binning. Mice were treated after the luminescent signal exceeded $1x10^8$ photons/mm^2, as this generally correlated with a tumor size of about 1.5-2 mm. Depending on the experiment, mice were injected either intravenously via the tail vein or subcutaneously at the nape of the neck with the materials of interest.

Flow cytometric analysis of tumors

Mice were sacrificed and tumors were removed and kept on ice in DMEM. Tumors were then dissociated using a mouse tumor dissociation kit (Miltenyi Biotec) according to manufacturer's instructions. Cells were filtered through a 35-micron filter to obtain a single cell suspension, washed thrice, and analyzed on a BD LSR II flow cytometer. Washes and stains were performed in PBS with 1% BSA and 2 mM EDTA.

Intravital imaging

Mice were injected with 150 μL of 1 μM CTX-PEG4-siRNA-Cy5.5. They were then anesthetized with 150 mg/kg ketamine and 10 mg/kg xylazine. A craniotomy was performed to expose the brain, and a glass cover slip was placed against the brain. The mouse was secured with laboratory tape and placed on the heated stage of an Olympus FV1000 Multiphoton confocal. After imaging the mouse was sacrificed. Images were processed with the Volocity software to create maximum intensity projections.

In vivo RNA knockdown

Mice were sacrificed, perfused with cold PBS, and tumors were removed into SPEX sample prep tubes and immediately frozen in liquid nitrogen. Tumors were then cryogenically ground to a fine powder using a Geno/Grinder 2000. About 3 mg of powdered tissue was resuspended in 500 µL of Tissue Homogenization Solution (Epicentre), and 50 micrograms of Proteinase K (Epicentre) was added. The mixture was incubated for 2 hours at 55 C with 800 rpm shaking in 1.5 mL tubes. Afterwards, the solution was further homogenized by sequential passage through 20, 22, 25, and 30 gauge needles. The homogenized solution was then assayed for mRNA using the Quantigene 2.0 mRNA assay (Affymetrix). In the analysis, AHA1 mRNA levels were normalized by ACTB mRNA levels to account for variations in cell loading.

References

1. Zhang J, Shakhnovich EI (2010) Optimality of mutation and selection in germinal centers. *PLoS Comput Biol* 6(6):e1000800.

2. Omuro A, DeAngelis LM (2013) Glioblastoma and Other Malignant Gliomas. *JAMA* 310(17):1842. Available at: http://www.ncbi.nlm.nih.gov/pubmed/24193082 [Accessed April 27, 2017].

3. Ho VKY, et al. (2014) Changing incidence and improved survival of gliomas. *Eur J Cancer* 50(13):2309–2318. Available at: http://www.sciencedirect.com/science/article/pii/S0959804914007187 [Accessed April 27, 2017].

4. Ostrom QT, et al. (2014) CBTRUS Statistical Report: Primary Brain and Central Nervous System Tumors Diagnosed in the United States in 2007-2011. *Neuro*

Oncol 16(suppl 4):iv1-iv63. Available at: https://academic.oup.com/neuro-oncology/article-lookup/doi/10.1093/neuonc/nou223 [Accessed April 27, 2017].

5. Devi GR (2006) siRNA-based approaches in cancer therapy. *Cancer Gene Ther* 13(9):819–829. Available at: http://www.nature.com/doifinder/10.1038/sj.cgt.7700931 [Accessed June 2, 2017].

6. Hannon GJ (2002) RNA interference. *Nature* 418(6894):244–251. Available at: http://www.nature.com/doifinder/10.1038/418244a [Accessed April 27, 2017].

7. Whitehead K a, Langer R, Anderson DG (2009) Knocking down barriers: advances in siRNA delivery. *Nat Rev Drug Discov* 8(2):129–38. Available at: http://www.ncbi.nlm.nih.gov/pubmed/19180106 [Accessed February 3, 2013].

8. Lorenzer C, Dirin M, Winkler A-M, Baumann V, Winkler J (2015) Going beyond the liver: Progress and challenges of targeted delivery of siRNA therapeutics. *J Control Release* 203:1–15. Available at: http://www.sciencedirect.com/science/article/pii/S0168365915000930 [Accessed February 19, 2015].

9. Tomar RS, Matta H, Chaudhary PM (2003) Use of adeno-associated viral vector for delivery of small interfering RNA. *Oncogene* 22(36):5712–5715. Available at: http://www.ncbi.nlm.nih.gov/pubmed/12944921 [Accessed April 27, 2017].

10. Khorev O, Stokmaier D, Schwardt O, Cutting B, Ernst B (2008) Trivalent, Gal/GalNAc-containing ligands designed for the asialoglycoprotein receptor. *Bioorg Med Chem* 16(9):5216–31. Available at: http://www.sciencedirect.com/science/article/pii/S0968089608002307 [Accessed

May 30, 2014].

11. Lyons SA, O'Neal J, Sontheimer H (2002) Chlorotoxin, a scorpion-derived peptide, specifically binds to gliomas and tumors of neuroectodermal origin. *Glia* 39(2):162–173. Available at: http://doi.wiley.com/10.1002/glia.10083 [Accessed April 27, 2017].

12. Veiseh M, et al. (2007) Tumor Paint: A Chlorotoxin:Cy5.5 Bioconjugate for Intraoperative Visualization of Cancer Foci. *Cancer Res* 67(14). Available at: http://cancerres.aacrjournals.org/content/67/14/6882 [Accessed April 27, 2017].

13. Kesavan K, et al. (2010) Annexin A2 is a molecular target for TM601, a peptide with tumor-targeting and anti-angiogenic effects. *J Biol Chem* 285(7):4366–74. Available at: http://www.jbc.org/content/285/7/4366.full [Accessed May 31, 2014].

14. Franklin HL, Miller DM, Hedges T, Perry J, Parrish-Novak J (2016) Clinical development of BLZ-100 for real-time optical imaging of tumors during resection. eds Pogue BW, Gioux S (International Society for Optics and Photonics), p 96960V. Available at: http://proceedings.spiedigitallibrary.org/proceeding.aspx?doi=10.1117/12.2224856 [Accessed April 27, 2017].

15. Wu C, et al. (2011) Design of Highly Emissive Polymer Dot Bioconjugates for In Vivo Tumor Targeting. *Angew Chemie Int Ed* 50(15):3430–3434. Available at: http://doi.wiley.com/10.1002/anie.201007461 [Accessed June 2, 2017].

16. Jewett JC, et al. (2010) Cu-free click cycloaddition reactions in chemical biology. *Chem Soc Rev* 39(4):1272. Available at: http://xlink.rsc.org/?DOI=b901970g

[Accessed June 2, 2017].

17. PONTÉN J, MACINTYRE EH (2009) LONG TERM CULTURE OF NORMAL AND NEOPLASTIC HUMAN GLIA. *Acta Pathol Microbiol Scand* 74(4):465–486. Available at: http://doi.wiley.com/10.1111/j.1699-0463.1968.tb03502.x [Accessed April 27, 2017].

18. Wang X, et al. (2006) Hsp90 cochaperone Aha1 downregulation rescues misfolding of CFTR in cystic fibrosis. *Cell* 127(4):803–15. Available at: http://www.ncbi.nlm.nih.gov/pubmed/17110338 [Accessed April 28, 2017].

19. Schneider B, et al. (2012) Targeted siRNA Delivery and mRNA Knockdown Mediated by Bispecific Digoxigenin-binding Antibodies. *Mol Ther Nucleic Acids* 1(9):e46. Available at: http://www.ncbi.nlm.nih.gov/pubmed/23344238 [Accessed April 28, 2017].

20. Chiu Y-L, Rana TM (2003) siRNA function in RNAi: a chemical modification analysis. *RNA* 9(9):1034–48. Available at: http://www.ncbi.nlm.nih.gov/pubmed/12923253 [Accessed May 17, 2017].

21. Nijhawan D, et al. (2012) Cancer vulnerabilities unveiled by genomic loss. *Cell* 150(4):842–54. Available at: http://www.ncbi.nlm.nih.gov/pubmed/22901813 [Accessed September 1, 2017].

22. Ozawa T, James CD (2010) Establishing intracranial brain tumor xenografts with subsequent analysis of tumor growth and response to therapy using bioluminescence imaging. *J Vis Exp* (41). Available at: http://www.ncbi.nlm.nih.gov/pubmed/20644517 [Accessed April 28, 2017].

Chapter 4: PSMA-Ligand conjugates

Overview

Prostate cancer is the second most common type of cancer worldwide (1). However, it is the fifth leading cause of mortality from cancer in men (1). Currently, incidence rates are rising around the world, especially in Asia and Europe, necessitating the need for better methods of diagnosing and treating prostate cancer (2).

Chemotherapeutics such as doxorubicin and paclitaxel have been shown to be effective against prostate cancer (3, 4). However, because they target rapidly-dividing cells, chemotherapy is highly toxic and induces a wide range of side effects, including neutropenia, organ damage, and hair loss (5). By using targeted therapy to increase the concentration of the chemotherapeutic in the tumor, lower doses can be used to kill the tumor while sparing healthy tissues. Thus, new methods of targeted delivery of chemotherapeutics to prostate cancer are urgently needed.

Prostate-specific membrane antigen (PSMA) is a binuclear zinc metallopeptidase that is normally expressed in prostate tissues and the nervous system (6). However, in malignant prostate cancers, especially androgen resistant cancers, PSMA is expressed at levels that increase with increasing cancer grade (7). Furthermore, PSMA expression has been found in cancers of the kidney, bladder, breast, colon, and Schwann cells as well(8, 9). Other work has demonstrated that PSMA is expressed in the neovasculature of solid tumors, but not the regular tissue vasculature (9, 10). Thus, because of these features, it has been used as an imaging agent for the diagnosis of prostate cancer (11–13).

To create imaging agents, PSMA-directed antibodies and aptamers have mainly been conjugated to PET and SPECT labels (11–14). Recently, a family of urea-based

small molecule inhibitors of PSMA have been found, and have been used as imaging agents as well (15, 16). Unlike antibodies and aptamers, these small molecule ligands have easier access to the tumor due to their smaller size. Furthermore, because of the structure of PSMA, large cargo can be conjugated to these urea-based molecules and still maintain activity of the inhibitor (17). Based on these observations, we decided to use these PSMA ligands to deliver chemotherapeutics to PSMA-expressing tumors.

PSMA Ligand conjugates

PSMA Ligand conjugates were synthesized by our collaborators at Moscow State University. Alex Majouga's laboratory synthesized the PSMA ligand. They also synthesized chemotherapeutic conjugates with doxorubicin and paclitaxel that were ligated with a hydrazine linker. The drug conjugates were first solubilized in DMSO, aliquoted, and kept at -20 C. Before usage, they were dissolved in a small amount (typically 5 µL) of Tween 20 to aid in solubilization. For experiments, they were diluted to a final Tween concentration of 2%. An example of one of the conjugates is shown in Figure 4.1.

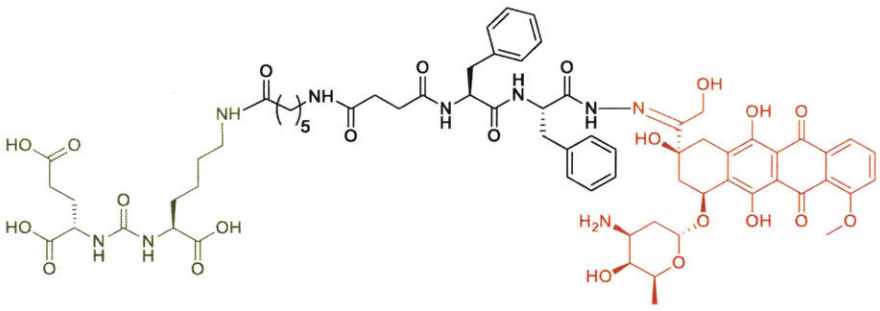

Figure 4.1. Example of PSMA ligand conjugate.
Urea-based PSMA ligand (green) is connected through a linker (black) to doxorubicin (red). These molecules were synthesized by Alex Majouga's laboratories.

PSMA ligand-chemotherapeutic conjugates do not lose their efficacy in vitro

In order to determine whether conjugates of PSMA ligands are capable of killing cancer cells, I tested the PSMA ligand-paclitaxel and PSMA-ligand doxorubicin conjugates in vitro on 22Rv1 cells (ATCC). This cell line is derived from a human prostatic carcinoma that was serially propagated in mice, and is known to express PSMA(18, 19). Compared to other prostate cancer cell lines, such as LNCaP, it grew faster and was easier to culture. The 22Rv1 cells were grown in RPMI with 10% FBS (Thermo Fisher) in Corning TC-treated culture flasks.

The results can be found in Figure 4.2 and Figure 4.3. For the paclitaxel conjugates, these results indicate that although the paclitaxel alone does appear to be slightly more potent, the addition of these targeting ligands using copper-catalyzed azide-alkyne cycloaddition does not affect the drug in a substantial manner. The ligand-targeted doxorubicin conjugates appear to be more potent than unconjugated doxorubicin.

However, these experiments also indicate that there was not a high degree of increased cytotoxicity from the conjugation. This indicates that the PSMA receptor is not rapidly transporting more of the chemotherapeutic into the cell. Since PSMA is a cell-surface enzyme that acts as a glutamate carboxypeptidase, we would not expect it to function as a transporter (6). However, *in vivo*, the conjugate could still have an effect as the conjugate could increase the local concentration of chemotherapeutic around the cells, increasing the rate of endocytosis and cell death.

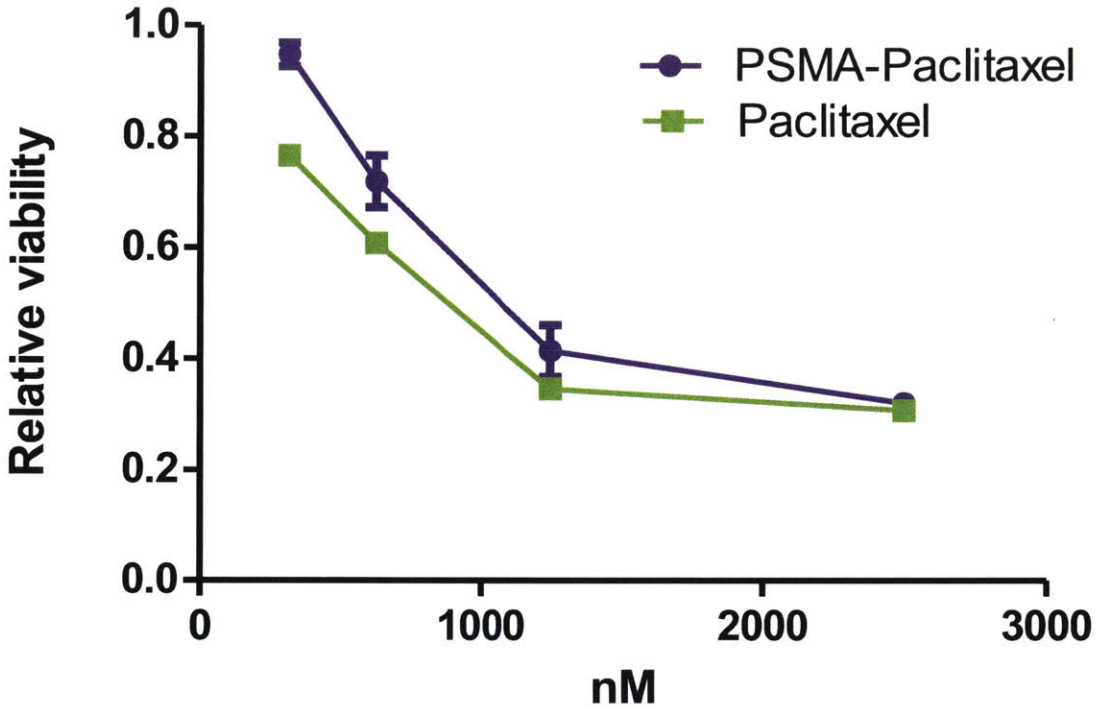

Figure 4.2. PSMA-Paclitaxel has comparable in vitro efficacy to paclitaxel. 22Rv1 cells that express PSMA were plated at a density of 25000 cells per well. The cells were treated with paclitaxel or conjugated paclitaxel at the specified concentrations for 96 hours. Cell viability was measured using the CellTiter-Glo assay (Promega). PSMA ligand-paclitaxel conjugates were synthesized by Alex Majouga's laboratory.

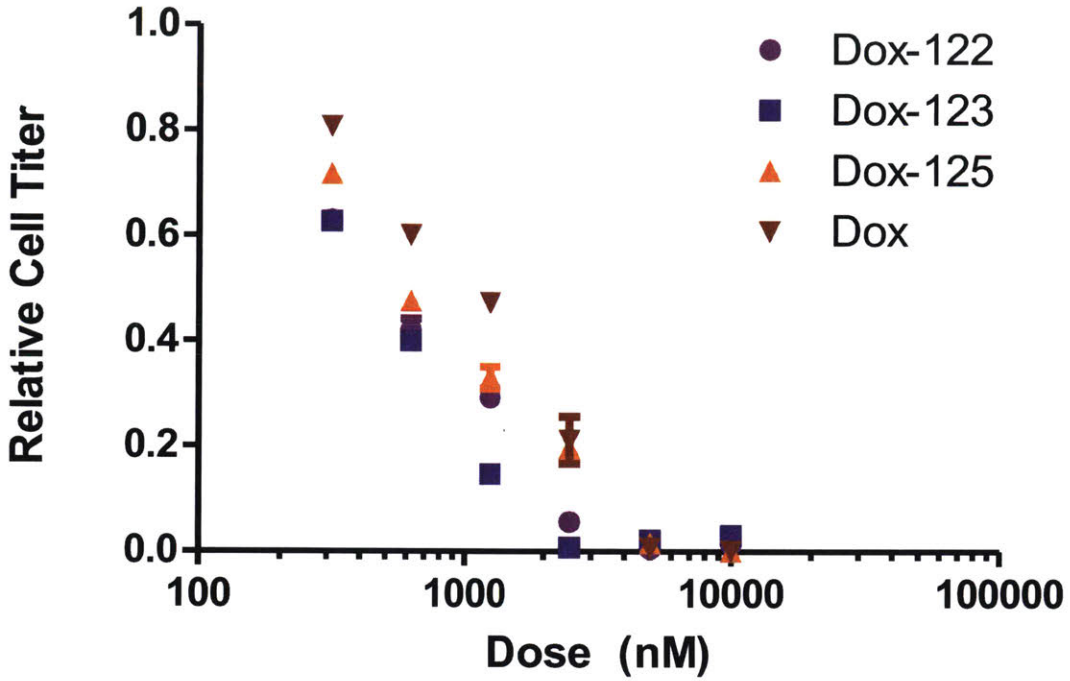

Figure 4.3. Dox and Dox-PSMA ligand conjugates have similar degrees of cytotoxicity.
22Rv1 cells that express PSMA were plated at a density of 25000 cells per well. The cells were treated with doxorubicin or conjugated doxorubicin at the specified concentrations for 96 hours. Cell viability was measured using the CellTiter-Glo assay (Promega). Dox-122, Dox-123, and Dox-125 are variants of the Dox-PSMA ligand conjugates that differ slightly in chemical structure. They were synthesized by Alex Majouga's laboratory.
In vivo testing of PSMA ligand paclitaxel conjugates

In order to determine whether there could be some *in vivo* activity in terms of targeted cell killing, I tested the PSMA ligand paclitaxel conjugates on nu/nu mice with subcutaneous flank 22Rv1 xenografts. We used the PSMA-Paclitaxel conjugates instead of the PSMA-Dox as Majouga's laboratory made sufficient PSMA-Paclitaxel to do longer-term animal experiments. Tumor induction was done with $2x10^6$ freshly isolated 22Rv1 cells kept on ice in 100 µL of PBS mixed with 100 µL of Matrigel that had been thawed

overnight at 4 C. The solution was injected into the left flank of nu/nu mice to establish the tumor. Tumor formation was monitored using calipers, and tumor volume was calculated using the formula $wxh^2x0.52$, where *w* is the major axis of the tumor and *h* is the minor axis. Treatment was initiated once the tumor reached a volume of 50 mm^3. This took approximately three weeks.

During the treatment, either conjugated or unconjugated drug was administered intraperitoneally very Monday, Wednesday, and Friday. Mice were monitored after injections for any toxicity. No severe adverse events were observed during the entire treatment period. Tumor size was measured every Monday, Wednesday, and Friday as well for 21 days. Mice were sacrificed after the experimental endpoint by CO_2 asphyxiation, and tumors were removed for analysis.

The results in terms of growth of tumor can be found in Figure 4.4. It should be noted that there was a very high degree of biological variation in terms of the tumor sizes, indicating that future experiments should be done with higher sample sizes. However, it is clear that untreated mice have much higher tumor volumes than either the paclitaxel or PSMA ligand-paclitaxel groups.

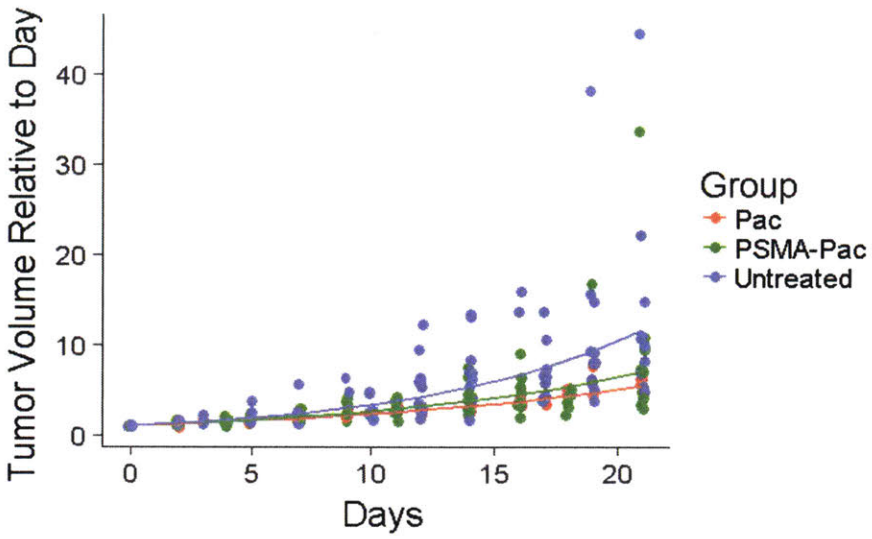

Figure 4.4. Tumor growth and variation across the different treatments. Tumor induction was performed on nu/nu mice with $2x10^6$ 22Rv1 cells mixed with Matrigel. Mice were treated when tumors reached 50 mm^3. 3 mg/kg PSMA ligand paclitaxel and paclitaxel were administered IP every M,W,F after treatment initiation. Both treatments were solubilized with 2% of Tween 20. Tumor volume measurements were performed using calipers, and tumor volume was calculated using the formula wxh2x0.52, where w is the major axis of the tumor and h is the minor axis. Relative tumor volumes were calculated by dividing the measured tumor volume on that day with the tumor volume when treatment was initiated. Sample sizes are as follows: untreated, 11; Pac, 4; PSMA-Pac, 6.

In order to overcome this variability and extract useful information from the data, I used a mixed effect model to estimate the tumor growth rate. First, the tumor volumes were log-transformed to reduce heteroscedasticity. Then, I fitted the data using Days and Treatment:Days as fixed effects, and used the individual as a random effect. A general linear hypothesis test was used to determine the effect size of the groups in terms of the doubling rate and to determine 95% confidence intervals for this measure. The doubling rate is plotted in Figure 4.5. Significant differences were found between the Untreated and the Pac-PSMA and PSMA groups ($p < 0.001$ for both) but not between the PSMA and Pac-PSMA groups ($p = 0.98$). Thus, we conclude that the PSMA ligand conjugate did not significantly reduce tumor burden any more than unconjugated PSMA.

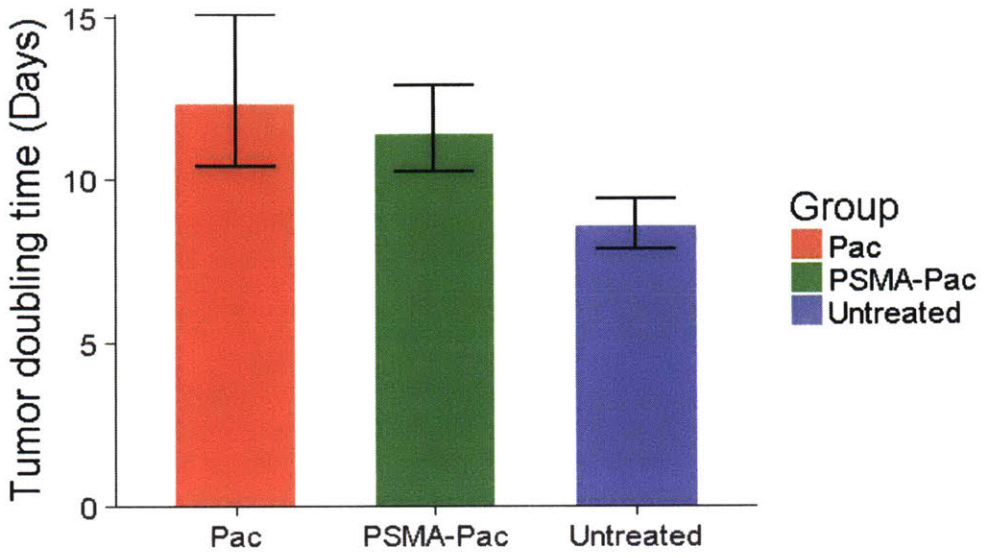

Figure 4.5. PSMA Paclitaxel and PSMA have similar levels of efficacy.
Tumor induction was performed on nu/nu mice with $2x10^6$ 22Rv1 cells mixed with Matrigel. Mice were treated when tumors reached 50 mm^3. PSMA ligand paclitaxel and paclitaxel were administered IP every M,W,F after treatment initiation. Both treatments were solubilized with 2% of Tween 20. Sample sizes are as follows: untreated, 11; Pac, 4; PSMA-Pac, 6. Tumor volume measurements were performed using calipers, and tumor volume was calculated using the formula wxh2x0.52, where w is the major axis of the tumor and h is the minor axis. Tumor doubling time was calculated using a linear mixed-effects model of the form log(Relative volume) ~ 1 + Treatment:Days + Days with a random individual effect. Generalized linear hypothesis testing was used to compute the tumor doubling time and the 95% confidence intervals (error bars shown).

The fact that the PSMA-paclitaxel conjugate did not significantly decrease tumor burden may be attributed to a variety of causes. One reason could be poor tumor vascularization. Because the tumors in this case were not well-vascularized (not many blood vessels were seen), it is likely that the PSMA-paclitaxel was unable to penetrate the tumor fully. Lack of drug penetration has been observed for other tumors due to increased intratumor pressure and solid stress, and it is well known that even small molecules find it difficult to penetrate tumors (20, 21). Although this is not an avoidable

problem, other xenograft models, such as LNCaP tumors, show higher degrees of vascularization, and perhaps would be more responsive to the conjugate.

Secondly, the dose used was fairly low in the context of other studies that have used paclitaxel in xenografts. Doses of up to 20 mg/kg have been used to allow for adequate response. Due to the limited amount of conjugate we received, I chose to dose at only 3 mg/kg to ensure that we would have enough for a larger number of mice (6 in the conjugate group and 3 in the control) over a period of three weeks. The time duration is important, as it is at the later stages of exponential growth of the tumors that the differences become clearer between the untreated and paclitaxel treated groups (see Figure 4.4). Hence, perhaps higher doses of the drug or more frequent dosing would result in better performance of the conjugate.

Lastly, tumor growth rates varied greatly among the mice, even in the untreated group. Although all mice were injected in the same method on the same day from the same batch of cells, the tumors behaved very differently. This could be due to the exponential nature of tumor growth: small changes in initial growth rate are amplified into large differences in tumor size due to the rapidly proliferating nature of tumor cells. However, because of this, sample sizes would have to be increased, perhaps to up to 15-20 mice per group in order to have sufficient power to detect differences from noisy data.

References

1. Torre LA, et al. (2015) Global cancer statistics, 2012. *CA Cancer J Clin* 65(2):87–108. Available at: http://www.ncbi.nlm.nih.gov/pubmed/25651787 [Accessed September 10, 2017].
2. Wong MCS, et al. (2016) Global Incidence and Mortality for Prostate Cancer:

Analysis of Temporal Patterns and Trends in 36 Countries. *Eur Urol* 70(5):862–874. Available at: http://www.ncbi.nlm.nih.gov/pubmed/27289567 [Accessed September 10, 2017].

3. Chiappino I, et al. (2007) Activity of Weekly Paclitaxel in Advanced Hormone-Refractory Prostate Cancer. *Am J Clin Oncol* 30(3):234–238. Available at: http://www.ncbi.nlm.nih.gov/pubmed/17551298 [Accessed September 10, 2017].
4. Sella A, et al. (1994) Phase II study of ketoconazole combined with weekly doxorubicin in patients with androgen-independent prostate cancer. *J Clin Oncol* 12(4):683–8. Available at: http://www.ncbi.nlm.nih.gov/pubmed/7512126 [Accessed September 11, 2017].
5. Iwamoto T (2013) Clinical Application of Drug Delivery Systems in Cancer Chemotherapy: Review of the Efficacy and Side Effects of Approved Drugs. *Biol Pharm Bull* 36(5):715–718. Available at: http://jlc.jst.go.jp/DN/JST.JSTAGE/bpb/b12-01102?lang=en&from=CrossRef&type=abstract [Accessed September 11, 2017].
6. Bařinka C, Rojas C, Slusher B, Pomper M (2012) Glutamate carboxypeptidase II in diagnosis and treatment of neurologic disorders and prostate cancer. *Curr Med Chem* 19(6):856–70. Available at: http://www.ncbi.nlm.nih.gov/pubmed/22214450 [Accessed September 10, 2017].
7. Bostwick DG, Pacelli A, Blute M, Roche P, Murphy GP (1998) Prostate specific membrane antigen expression in prostatic intraepithelial neoplasia and adenocarcinoma: a study of 184 cases. *Cancer* 82(11):2256–61. Available at: http://www.ncbi.nlm.nih.gov/pubmed/9610707 [Accessed September 10, 2017].

8. Kinoshita Y, et al. (2006) Expression of Prostate-Specific Membrane Antigen in Normal and Malignant Human Tissues. *World J Surg* 30(4):628–636. Available at: http://www.ncbi.nlm.nih.gov/pubmed/16555021 [Accessed September 10, 2017].

9. Haffner MC, et al. (2009) Prostate-specific membrane antigen expression in the neovasculature of gastric and colorectal cancers. *Hum Pathol* 40(12):1754–1761. Available at: http://www.ncbi.nlm.nih.gov/pubmed/19716160 [Accessed September 10, 2017].

10. Chang SS, et al. (1999) Five different anti-prostate-specific membrane antigen (PSMA) antibodies confirm PSMA expression in tumor-associated neovasculature. *Cancer Res* 59(13):3192–8. Available at: http://www.ncbi.nlm.nih.gov/pubmed/10397265 [Accessed September 10, 2017].

11. Bander NH, et al. (2005) Phase I Trial of ^{177} Lutetium-Labeled J591, a Monoclonal Antibody to Prostate-Specific Membrane Antigen, in Patients With Androgen-Independent Prostate Cancer. *J Clin Oncol* 23(21):4591–4601. Available at: http://www.ncbi.nlm.nih.gov/pubmed/15837970 [Accessed September 10, 2017].

12. Holland JP, et al. (2010) 89Zr-DFO-J591 for ImmunoPET of Prostate-Specific Membrane Antigen Expression In Vivo. *J Nucl Med* 51(8):1293–1300. Available at: http://www.ncbi.nlm.nih.gov/pubmed/20660376 [Accessed September 10, 2017].

13. Rockey WM, et al. (2011) Synthesis and radiolabeling of chelator–RNA aptamer bioconjugates with copper-64 for targeted molecular imaging. *Bioorg Med Chem* 19(13):4080–4090. Available at: http://www.ncbi.nlm.nih.gov/pubmed/21658962 [Accessed September 10, 2017].

14. Murphy GP, et al. (1997) Comparison of serum PSMA, PSA levels with results of

Cytogen-356 ProstaScint scanning in prostatic cancer patients. *Prostate* 33(4):281–5. Available at: http://www.ncbi.nlm.nih.gov/pubmed/9397201 [Accessed September 10, 2017].

15. Kozikowski AP, et al. (2001) Design of remarkably simple, yet potent urea-based inhibitors of glutamate carboxypeptidase II (NAALADase). *J Med Chem* 44(3):298–301. Available at: http://www.ncbi.nlm.nih.gov/pubmed/11462970 [Accessed September 10, 2017].
16. Banerjee SR, et al. (2008) Synthesis and Evaluation of Technetium-99m- and Rhenium-Labeled Inhibitors of the Prostate-Specific Membrane Antigen (PSMA). *J Med Chem* 51(15):4504–4517. Available at: http://www.ncbi.nlm.nih.gov/pubmed/18637669 [Accessed September 10, 2017].
17. Mesters JR, et al. (2006) Structure of glutamate carboxypeptidase II, a drug target in neuronal damage and prostate cancer. *EMBO J* 25(6):1375–1384. Available at: http://www.ncbi.nlm.nih.gov/pubmed/16467855 [Accessed September 10, 2017].
18. Sramkoski RM, et al. (1999) A new human prostate carcinoma cell line, 22Rv1. *Vitr Cell Dev Biol - Anim* 35(7):403–409. Available at: http://www.ncbi.nlm.nih.gov/pubmed/10462204 [Accessed September 9, 2017].
19. Regino CAS, et al. (2009) Preclinical evaluation of a monoclonal antibody (3C6) specific for prostate-specific membrane antigen. *Curr Radiopharm* 2(1):9–17. Available at: http://www.ncbi.nlm.nih.gov/pubmed/20047017 [Accessed September 9, 2017].
20. Minchinton AI, Tannock IF (2006) Drug penetration in solid tumours. *Nat Rev Cancer* 6(8):583–592. Available at:

http://www.nature.com/doifinder/10.1038/nrc1893 [Accessed September 10, 2017].

21. Stylianopoulos T, et al. (2013) Coevolution of solid stress and interstitial fluid pressure in tumors during progression: implications for vascular collapse. *Cancer Res* 73(13):3833–41. Available at: http://www.ncbi.nlm.nih.gov/pubmed/23633490 [Accessed September 9, 2017].